HERIOT-WATT UNIVERSITY

MASTERS THESIS

Supercontinuum Generation in Orientation-Patterned Gallium Phosphide

Author:
Anchit Shrikant Srivastava

Supervisor:
Derryck T. Reid

A thesis submitted in fulfilment of the requirements
for the degree of MSc. by research

in the

Institute of Photonics and Quantum Sciences,
School of Engineering and Physical Sciences

June 2020

Declaration of Authorship

I, Anchit Shrikant Srivastava, declare that this thesis titled, 'Supercontinuum Generation in Orientation-Patterned Gallium Phosphide' and the work presented in it is my own. I confirm that this work submitted for assessment is my own and is expressed in my own words. Any uses made within it of the works of other authors in any form (e.g., ideas, equations, figures, text, tables, programs) are properly acknowledged at any point of their use. A list of the references employed is included.

Signed: Anchit Srivastava

Date: 30-06-2020

Abstract

A supercontinuum from the blue/green to the red is generated by pumping orientation-patterned gallium phosphide crystal by femtosecond pulses from Yb:fibre laser. Experimentally, the supercontinuum is generated by focusing 32 nJ 100 fs pulses at 1040 nm into the OPGaP crystal, to a focus of w_0=25 μm. Using a nonlinear envelope equation model developed in this work, a combine action of $\chi^{(2)}$ and $\chi^{(3)}$ nonlinearities is shown to be the origin of the supercontinuum generation. The modelling implies that high-order parametric gain pumped by the second-harmonic light of the laser and seeded by self-phase-modulated sidebands is responsible. The results represent the first time a visible supercontinuum has been generated in a bulk material using a low-energy high-repetition rate femtosecond laser.

Research Thesis Submission

Please note this form should be bound into the submitted thesis.

Name:	Anchit Shrikant Srivastava		
School:	EPS/IPAQS		
Version: *(i.e. First, Resubmission, Final)*	Final	Degree Sought:	Msc by research in Physics

Declaration

In accordance with the appropriate regulations I hereby submit my thesis and I declare that:

1. The thesis embodies the results of my own work and has been composed by myself
2. Where appropriate, I have made acknowledgement of the work of others
3. The thesis is the correct version for submission and is the same version as any electronic versions submitted*.
4. My thesis for the award referred to, deposited in the Heriot-Watt University Library, should be made available for loan or photocopying and be available via the Institutional Repository, subject to such conditions as the Librarian may require
5. I understand that as a student of the University I am required to abide by the Regulations of the University and to conform to its discipline.
6. I confirm that the thesis has been verified against plagiarism via an approved plagiarism detection application e.g. Turnitin.

ONLY for submissions including published works

Please note you are only required to complete the Inclusion of Published Works Form (page 2) if your thesis contains published works)

7. Where the thesis contains published outputs under Regulation 6 (9.1.2) or Regulation 43 (9) these are accompanied by a critical review which accurately describes my contribution to the research and, for multi-author outputs, a signed declaration indicating the contribution of each author (complete)
8. Inclusion of published outputs under Regulation 6 (9.1.2) or Regulation 43 (9) shall not constitute plagiarism.

* *Please note that it is the responsibility of the candidate to ensure that the correct version of the thesis is submitted.*

Signature of Candidate:	Anchit Srivastava	Date:	30-06-2020

Submission

Submitted By *(name in capitals):*	ANCHIT SHRIKANT SRIVASTAVA
Signature of Individual Submitting:	Anchit Srivastava
Date Submitted:	30-06-2020

For Completion in the Student Service Centre (SSC)

Limited Access	Requested	Yes		No		Approved	Yes		No	
E-thesis Submitted ***(mandatory for final theses)***										
Received in the SSC by *(name in capitals):*						Date:				

Inclusion of Published Works

Please note you are only required to complete the Inclusion of Published Works Form if your thesis contains published works under Regulation 6 (9.1.2)

Declaration

This thesis contains one or more multi-author published works. In accordance with Regulation 6 (9.1.2) I hereby declare that the contributions of each author to these publications is as follows:

Citation details	Marius Rutkauskas, Anchit Srivastava, and Derryck T. Reid, "Supercontinuum generation in orientation-patterned gallium phosphide," Optica 7, 172-175 (2020)
Author 1 & 2	Experimental measurement and characterisation
Author 3	Numerical simulation
Signature:	Anchit Srivastava
Date:	30-06-2020

Acknowledgements

I am very grateful to my parents for their constant support and guidance, which has kept me on the path to follow my passion.

Firstly, I would like to thank my research advisor, Professor Derryck Reid, without his support, the work presented in this thesis would not have been possible. His guidance and profundity in scientific knowledge have helped me grow as a researcher. He has always given me the freedom to work on projects which I like. Even when I had to step away from my PhD in the first year due to personal reasons, he understood and supported me to pursue my interest and also encouraged me to write down this thesis. I would also like to thank Yoann Altmann for his guidance and useful discussion during my time there.

When I arrived in Edinburgh, from the first day, Oguzhan made me feel like home and was like a mentor to me. I cannot thank Marius enough, as it is because of him, I picked up a lot of valuable skills in the lab. It was a pleasure to work with him and I greatly enjoyed our discussions over a coffee. My fellow group mates deserve a mention, especially Shan and Pablo for their valuable discussions and for being there when things weren't going well. I can confidently say that Shan is the sweetest person in the division but with very less drinking abilities.

Speaking of drinking, I cannot forget the Friday pub sessions where I met most of my fellow PhD students which later became part of my family outside the lab. I will miss Edinburgh and with it Max's drunk trash talk, another Max's English banter, Chris's pessimism and Lara's apfelstrudel. Lastly, I would like to thank my dear Natalia who made my life joyous and without whom this journey wouldn't have been possible in the first place.

Contents

List of Figures

Chapter 1

Introduction

1.1 Overview

There is a huge interest in developing supercontinuum sources due to its application in optical tomography [1], pulse compression [2], precision metrology [3], [4], and spectroscopy [5]. In these examples, the broadband coherent light is generated by pumping at a wavelength close to the near-zero dispersion regime. Fibre-based methods use this mechanism of dispersion tuning [6-10] to generate supercontinuum. The primary mechanism behind the supercontinuum generation here is SPM, FWM, soliton propagation and modulation instability. Depending on the type of fibre, the interplay between dispersion and nonlinearity can be used to tune the output spectra [6]–[8]. Another way of generating coherent supercontinuum is by using waveguides and integrated photonics. The on-chip based platforms include silica [9], silicon [10], [11], silicon nitride [12], [13], and chalcogenide [14], [15].

The quasi-phasematching technique is used in nonlinear optics to phase match different nonlinear processes. It is a powerful technique for generating, amplifying and broadening light. It uses engineered materials to phase match different nonlinear process with higher efficiency which was not possible due to conventional phasematching technique. Also, quasi-phasematching make it possible even for high-order nonlinear processes in $\chi^{(2)}$ materials to access substantial effective nonlinear coefficients. Early work in periodically poled lithium niobate (PPLN) demonstrated that this facility when combined with the high intensities available within guided-wave devices, enabled a form of supercontinuum generation that exploited multiple cascaded and high-order three-wave interactions to generate supercontinua [16]. This approach has since been refined both theoretically [17] and experimentally [18] to deliver greater control of such processes, but it has remained limited to waveguide devices, and principally to the material lithium niobate.

Engineerable phase matching in semiconductors like orientation-patterned gallium arsenide (OPGaAs) [19] and orientation-patterned gallium phosphide (OPGaP) [20] has enabled the demonstration of highly efficient ultra-broadband or extremely tunable femtosecond optical parametric oscillators [21], [22]. In particular, OPGaP combines transparency extending well into the visible region with a high nonlinear coefficient ($d_{14} = 70.6pm/V$) [23] that results in a nonlinear figure of merit (d_{eff}^2/n^3) 3 times that of PPLN [23]. When such a high nonlinear coupling is available along with a strong driving field, many high-order processes become relatively efficient in quasi-phasematched media; for example, the first report of optical parametric oscillation in-OPGaP observed ninth-order visible light generation using narrow-linewidth nanosecond pump pulses [23].

The main aim of this thesis to understand the principle processes acting to form supercontinuum in quasi-phasematched OPGaP crystal. In this chapter, I introduce fundamental concepts in nonlinear optics. Starting with Maxwell's equation, we then explain polarization and its contribution in second and third-order nonlinear processes. Later, I introduce quasi-phasematching to discuss the optical and properties of OPGaP crystal and role of achieving the second-order nonlinear process. In Chapter 2 I discuss the main processes i.e. dispersion and Kerr nonlinearity involved in supercontinuum generation. In brief, we also discuss the origins of cascaded $\chi^{(2)}$ effects. In Chapter 3 I introduce nonlinear envelope equations (NEE) to simulate the effect of quadratic and cubic nonlinearities. Finally, in Chapter 4, I present experimental details and compare the results with numerical modelling.

1.2 From Maxwell's equation to nonlinear optics

Before understanding the nonlinear polarization, it is essential to take a look at Maxwell's equations which govern all electromagnetic waves and light matter interaction

$$\nabla \cdot \mathbf{D} = \rho \tag{1.1a}$$

$$\nabla \cdot \mathbf{B} = 0 \tag{1.1b}$$

$$\nabla \times \mathbf{E} = -\frac{\partial \mathbf{B}}{\partial t} \tag{1.1c}$$

$$\nabla \times \mathbf{H} = \mathbf{J} + \frac{\partial \mathbf{D}}{\partial t} \tag{1.1d}$$

Here bold font indicates vector quantities and italic font scalar quantities. All quantities depend on the spatial co-ordinate $r(x,y,z)$ and time t. In these equations, $\mathbf{E}$ and $\mathbf{H}$ are electric and magnetic field respectively, $\mathbf{D}$ is the electric displacement and $\mathbf{H}$ is the magnetic induction, ρ and $\mathbf{J}$ are the electric charge density and electric current density respectively. $\mathbf{D}$ and $\mathbf{B}$ are related to $\mathbf{E}$ and $\mathbf{H}$ via the constitutive relations which are based on the medium responses to electric

and magnetic field:

$$\mathbf{B} = \mu_0 \mathbf{H} + \mathbf{M} \tag{1.2a}$$

$$\mathbf{D} = \varepsilon_0 \mathbf{E} + \mathbf{P} \tag{1.2b}$$

where ε_0 is the permittivity of free space, $\mathbf{P}$ is the polarization, μ_0 is the permeability of free space and $\mathbf{M}$ is the magnetization. In this work, the dielectric medium is charge free, i.e $\rho = 0$ and since the medium is non-magnetic, $\mathbf{M} = 0$.

1.2.1 Nonlinear polarization

A medium produces an optical response to an oscillating electric field vector, $\mathbf{E}$ travelling through it. The response is called the "polarisation", $\mathbf{P}$ and is used to describe an electromagnetic wave propagating through a media. The role of polarization can be understood using the non-linear wave equation for homogeneous and isotropic media [24], where the second derivative of the polarization term $\mathbf{P}$ is a source term indicating emission of radiation by accelerating charges. We use Maxwell's equations to derive the wave equation. By taking the curl of Equation 1.1d and inserting into Equation 1.1c, we arrive at

$$\nabla^2 \mathbf{E} - \frac{1}{c^2} \frac{\partial^2 \mathbf{E}}{\partial t^2} = \frac{1}{\varepsilon_0 c^2} \frac{\partial^2 \mathbf{P}}{\partial t^2} \tag{1.3}$$

The polarization is given by:

$$\mathbf{P} = \varepsilon_0 \, \chi^{(1)} \, \mathbf{E}(t) \tag{1.4}$$

Where, χ is the nonlinear susceptibility tensor and for simplicity, $\mathbf{E}$ and $\mathbf{P}$ are considered scalar quantities. Also, the time dependent t of the polarization is assumed to be instantaneous. In general, the polarization term can be expressed as a power series expansion of the field strength $\mathbf{E}$

$$\mathbf{P} = \varepsilon_0 \, [\chi^{(1)} \, \mathbf{E}(t) + \chi^{(2)} \, \mathbf{E}^2(t) + \chi^{(3)} \, \mathbf{E}^3(t) + \cdots] \tag{1.5}$$

The quantity $\chi^{(1)}$ is called the linear optical susceptibility whereas, the quantities $\chi^{(2)}$ and $\chi^{(3)}$ are known as the nonlinear optical susceptibilities respectively.

In the linear regime, the polarization induced in the medium is linear as the dipoles oscillates harmonically. Thus, this can only give rise to phase delay or absorption which are frequency dependent but not intensity dependent. The induced polarization in the nonlinear regime is beyond the linear regime such that they oscillate anharmonically. This results in the nonlinear response of the electric field. $\mathbf{P}$ further can be split into linear and nonlinear part:

$$\mathbf{P} = \mathbf{P}_L + \mathbf{P}_{NL} \tag{1.6}$$

$$\mathbf{P} = \varepsilon_0 \chi^{(1)} \mathbf{E}(t) + \varepsilon_0 [\chi^{(2)} \mathbf{E}^2(t) + \chi^{(3)} \mathbf{E}^3(t) + \cdots] \tag{1.7}$$

In the total polarization, the linear term is dominant and all the higher order terms are small perturbations when compared with is linear term.

1.2.2 Second order process

When only $\chi^{(2)}$ is considered among the other higher order terms from Equation (1.7), then

$$\mathbf{P}^{(2)} = \varepsilon_0 \chi^{(2)} \mathbf{E}^2(t) \tag{1.8}$$

is known as the second order polarization. $\chi^{(2)}$ is responsible for all the second order nonlinear optical interactions and can only take place in a noncentrosymmetric medium [25], i.e. crystals which do not show inversion symmetry. Considering the scalar field approximation and that the incident field is superposition of two different frequencies ω_1 and ω_2, the electric field is given by:

$$\mathbf{E}(t) \propto \mathbf{E}_1 e^{(-i\omega_1 t)} + \mathbf{E}_1^* e^{(i\omega_1 t)} + \mathbf{E}_2 e^{(-i\omega_2 t)} + E_2^* e^{(i\omega_2 t)} \tag{1.9}$$

Now, solving the Equation (1.8) by using this definition of the electric field, the resulting second order nonlinear polarization term may be written as:

$$P^{(2)} = \underbrace{P^{(2)}(2\omega_1 + P^{(2)}(2\omega_2)}_{\text{SHG}} + \underbrace{P^{(2)}(\omega_1 + \omega_2)}_{\text{SFG}} + \underbrace{P^{(2)}(\omega_1 - \omega_2)}_{\text{DFG}} + \underbrace{P^{(2)}(0)}_{\text{OR}} \tag{1.10}$$

The second order nonlinear polarization gives rise to different second order processes such as second harmonic generation (SHG), sum frequency generation (SFG), difference frequency generation (DFG), optical rectification (OR), etc. There are many combinations of these interactions which are possible but not all processes act at the same time. At a given time, only one process can be efficient. The selectivity and the efficiency of the process is determined by the phase matching condition which will be discussed later in this chapter.

1.2.3 Third order process

Third order nonlinear interactions can occur for both centrosymmetric and noncentrosymmetric media [26].

$$P^{(3)} = \varepsilon_0 \chi^{(3)} \mathbf{E}^3(t) \tag{1.11}$$

The resulting third order nonlinear polarization term is quite cumbersome as the term $E(t)^3$ has 44 components with many different frequencies. Hence, considering a case where a scalar

applied field is given by $E(t) = Acos\omega t$, then the third order nonlinear polarization is expressed as [24]:

$$P^{(3)} = \underbrace{\frac{1}{4}\varepsilon_0\chi^{(3)}A^3cos3\omega t}_{THG} + \frac{3}{4}\varepsilon_0\chi^{(3)}A^3cos\omega t. \tag{1.12}$$

The first term indicates a third harmonic generation (THG) process where a frequency of 3ω is generated when the incident field is of the frequency ω.

The second term describes an effect where the nonlinear polarization induces a change in local refractive index due to the incident field at ω. The nonlinearity is represented as:

$$n = n_0 + n_2 I \tag{1.13}$$

where, n_0 is the linear refractive index, n_2 is the local refractive index and I is the intensity of the incident field. The intensity dependent refractive index is an essential process for generating the supercontinuum and will be discussed more in the later chapters.

1.2.4 Phase matching

As seen earlier, many different nonlinear interactions can take place inside a medium but not all act at once. To efficiently select a process, one needs to understands the process of phase matching. We know that the nonlinear processes are related to each other via the law of conservation of energy but they also need to satisfy conservation of momentum $\hbar_p k = \hbar_s k + \hbar_i k$ and thereby reducing the number of allowed interactions. Physically, the need for phase matching arises because of dispersion in the refractive index of a material [27] [28] and due to the fact that nonlinear conversion is limited by different factors such as material availability and properties like transmission, thermal and mechanical properties,damage threshold etc. All of these factors must be satisfied in order to have an efficient interaction in a medium. As $P_{NL} << P_L$, noticeable nonlinear effects can only be observed when the incident field is propagated through a fairly long interaction length in a medium when the phase matching condition is satisfied, meaning that that the wavevector mismatch is

$$\Delta k = 0 \tag{1.14}$$

There are two techniques to make $\Delta k = 0$, namely birefringent phase matching and quasi phase matching. The first method uses birefringence of the nonlinear material to phase match the process. In this type of phase matching, different polarizations see different refractive indexes which results in waves traveling at distinct speeds. Depending on the value of Δk, two solutions are possible. One is the phase matching condition where the gain is exponential and the other when the phase matching condition is nonzero, in such case, the gain is oscillatory. To understand this, we can look at the second harmonic generation case illustrated below, where

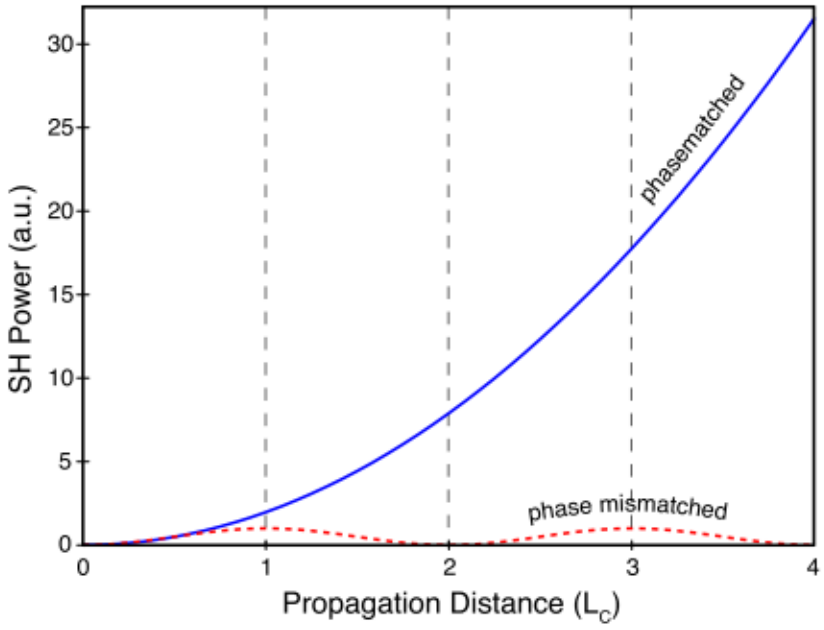

FIGURE 1.1: Second harmonic generation power as a function of propagation distance for a phase matched and phase mismatched process. Figure from [29]

$\omega_{SH} = 2\omega_{FH}$. In birefringent phase matching, both the fundamental and the second harmonic travel with the phase velocity $v_p = \omega/k$ through the nonlinear medium, and as a result transfer of energy from one wave to another is efficient as the wavevector mismatch is minimum. Wavevector mismatch arises due to the difference in phase velocity between the fundamental and second harmonic wave and the mismatch is given by $\Delta k = k_{SH} - 2k_{FH}$. As a result, after propagating the L_c distance, the phase difference between both the waves will by π and will interfere destructively. This can be seen in Figure 1.1. The overall power will flow back to the fundamental wave and the distance at which this reversal happens is called the coherence length ($L_c = \pi/\Delta k$).

Quasi phasematching utilises the periodic phase shift to obtain $\Delta k = 0$. Unlike birefringence phase matching, QPM allows the oscillatory feature of $\Delta k \neq 0$ but resets the wavevector mismatch to 0 when relative phase mismatch goes to π multiple of coherence length. This is achieved by reversing the sign of the nonlinear coefficient every L_c, thereby minimizing the destructive interference among second harmonic components and keeping the energy flowing from fundamental to the second harmonic. The phase mismatch now corresponds to

$$\Delta k = k_{SH} - 2k_{FH} - k_{QPM} \tag{1.15}$$

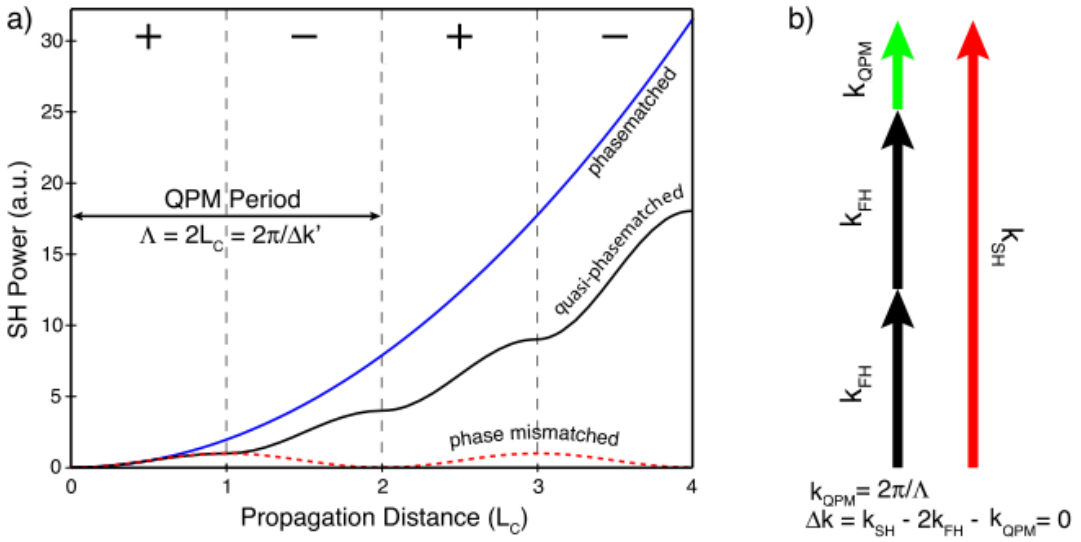

FIGURE 1.2: a) Second harmonic generation power as a function of propagation distance for a phase matched, phase mismatched and quasi phase matched process. b)Momentum conservation for a collinear SHG for a quasi phase matched process. Figure adapted from [29]

where, k_{QPM} is called the QPM grating vector and is introduced to sum the effective phase mismatch to zero. The QPM period is given by $\Lambda = 2L_c$

$$k_{QPM} = \frac{2\pi}{\Lambda} = \frac{\pi}{L_c} \tag{1.16}$$

The sign reversal in QPM is achieved through periodic poling or through orientation patterning [24] like the OPGaP. QPM has several advantages over birefringence phase matching. It allows noncritical phase matching at convenient temperatures and also extends utility of existing materials. The periodic variation of the nonlinear coefficient can be represented by a Fourier series expansion

$$\tilde{d}(z) = \sum_{m=-\infty}^{\infty} d_m e^{jK_m z}; \; K_m = \frac{2\pi\, m}{\Lambda} \tag{1.17}$$

For binary sign reversal, d_m is

$$d_m = \frac{2}{m\pi} sin(m\pi D) \tag{1.18}$$

Where D is the duty cycle of the periodic reversal and m is the phase matching order. For first-order quasi phasematching, m=1 and D=1/2 (50% duty cycle).

1.3 Orientation-patterned gallium phosphide (OPGaP)

Gallium phosphide has large optical nonlinearities (71 pm/V @ 1.064 μm) along with wide transparency range (0.55 - 12 μm) and high thermal conductivity (1.1 W/cm.K) [30]. Additionally, GaP has a low two-photon absorption coefficient at 1μm[31] resulting in low optical damage by high pump powers at this wavelength. Due to all these factors, GaP is suitable material for quadratic nonlinear interactions. With the help of quasi-phasematching, GaP can be used in a practical wavelength region along with efficient nonlinear conversion.

1.3.1 OPGaP fabrication and structure

The OPGaP crystal was fabricated using the all epitaxial processing technique which was originally designed for the fabrication of OP-GaAs structure [19][32][33]. The OPGaP crystal used in this work was developed by Peter Schunemann (BAE Systems). The complete description of the process is given in this paper [34]. Polar on nonpolar molecular beam epitaxy (MBE) was used to procduce a III-V semiconductor layer. The semiconductor layer was inverted relative to the substrate layer. The whole process was initiated with around 75nm undoped GaP substrate on which several buffer and smoothing layers were grown of a 200 nm thick GaP layers. The surface layer was patterned with a multi grating mask using photolithography technique and alternating domains were etched in Boron trichloride solution down to the starting substrate. To fill the leftover gaps from the photolithography, MBE was used again with non-inverted GaP. The output is a 2μm thin structure with alternating GaP orientation. Subsequently, the OPGaP template was loaded into a low pressure vapor phase epitaxy (HVPE) reactor to extend the structure. Figure 1.3 shows the polished and etched cross-sections of the OPGaP crystal samples used for the required phase matching in this thesis. Exemplary parallel and vertical domain propagation growth was achieved up to 150μm. Crystal lengths of 1 mm were diced and polished from the wafer. Lastly, anti-reflection coatings for near to mid-infrared wavelengths (1.02-1.06, 1.15-1.35 and 5–12 μm) were applied.

1.3.2 Quasi-phasematching in OPGaP

OPGaP is a polycrystalline QPM semiconductor of the group III-V which allows the use of a 1μm laser as pump due to its low two-photon absorption. Its high nonlinear coefficient at 1μm is 70.6 pm/V. The domain grating pattern enables the desired tuning parameter to cover the materials full transparency range.

The material's full transparency window which can be seen from the Figure 1.4 [35].

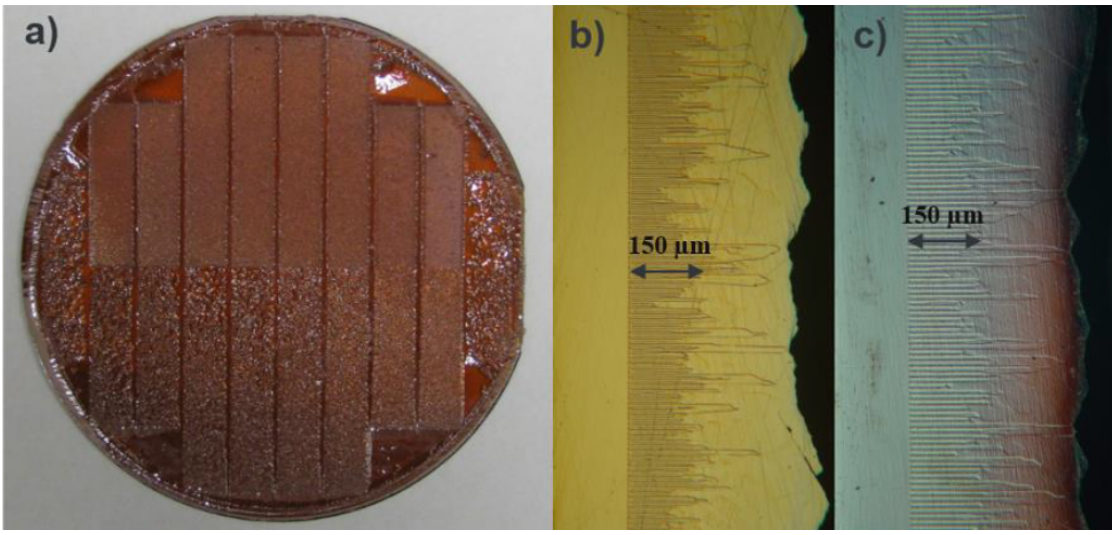

FIGURE 1.3: (a) The layout domain regions on the 75mm OPGaP wafer with cross sections revealing the domain period growth. The right part of the figure shows a diced and anti-reflection coated crystals of (b) 24.5μm and (c) 27μm [34].

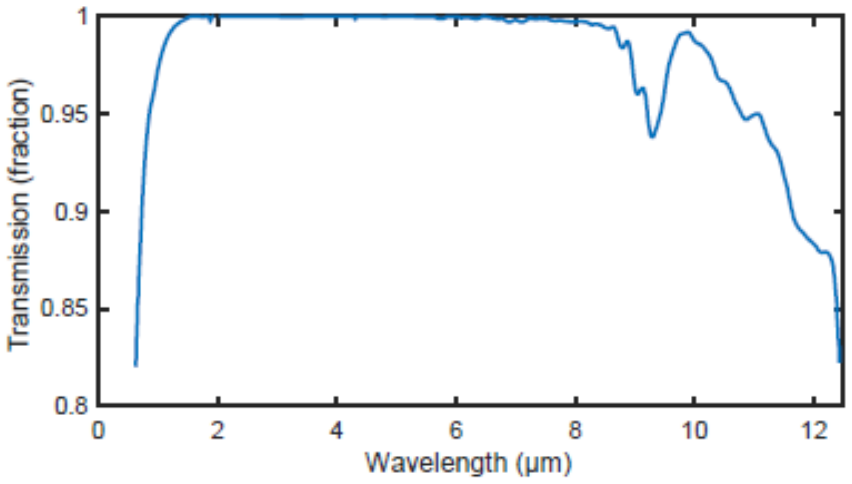

FIGURE 1.4: Transmission of 1mm OPGaP crystal.

The Sellmeier equations which governs the refractive index of the GaP as a function of wavelength is given by [36]:

$$n^2(\lambda) = 1 + \frac{A_1\lambda^2}{\lambda^2 - A_2^2} + \frac{B_1\lambda^2}{\lambda^2 - B_2^2} + \frac{C_1\lambda^2}{\lambda^2 - C_2^2} + \frac{D_1\lambda^2}{\lambda^2 - D_2^2} \tag{1.19}$$

where n is the refractive index, λ is wavelength in μm and A,B,C,D are experimentally determined Sellmeier coefficients. But the Sellmier equation used in this thesis is based on the work of Guha [36] and incorporates for wavelengths from 0.7 to 12.5 μm and temperature from

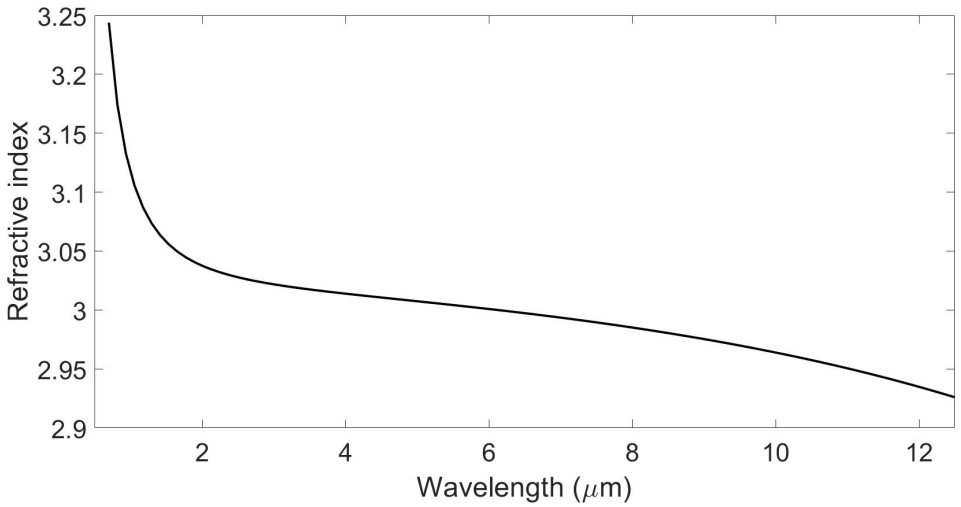

FIGURE 1.5: Refractive index of gallium phosphide obtained from the Sellmeier equation of [36]

78-450K. The equation reads as:

$$n^2 = A(T) + \frac{B(T)}{\lambda^2 - C} + \frac{D(T)}{\lambda^2 - E} \tag{1.20}$$

where, the parameter A and E were found for each temperature and the values of A,B,C and D were fitted to quadratic expression in T with better accuracy. The Figure 1.5 shows the refractive index of OPGaP in the transparency window.

Chapter 2

Processes involved in a supercontinuum generation in a quasi-phasematched crystal

Supercontinuum generation involves multiple processes which interact dynamically to generate new frequencies. The newly generated frequencies depend strongly on the medium of the interaction and the interplay between dispersion and nonlinearities. In this chapter I describe the effects which are responsible for generating the supercontinuum in a QPM crystal.

2.1 Dispersion

Dispersion is a linear effect which describes the dependence of the velocity of light at different wavelengths. Dispersion can arise due to the frequency-dependent refractive index of the material called as material dispersion whereas geometric structure of a waveguide causes waveguide dispersion.

optical resonances occur at different frequencies over the whole electromagnetic spectrum, and as a result the index of refraction varies. Figure 2.1 illustrates a typical distribution of resonances, with electronic resonances in the UV; vibrational and rotational resonances in the IR, and core electronic resonances occur in the x-ray region. The region between the normal dispersion at which resonances occur is called the anomalous dispersion region and can be seen as multiple peak and valley over the spectrum in Figure 2.1. The refractive index decreases in the anomalous region.

In nonlinear optics, β is known as the propagation constant which describes the phase shift of the pulse as it propagates. It is important to understand the behaviour of $\beta(\omega)$ for the generation of

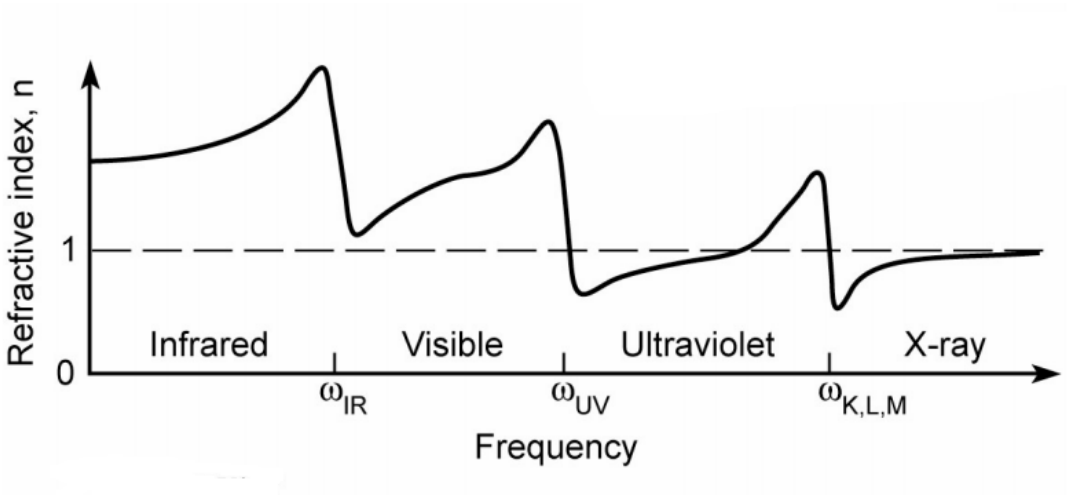

FIGURE 2.1: Illustration of refractive index vs frequency.

supercontinuum. Using a Taylor series expansion to expand $\beta(\omega)$ we get a generalised equation for the propagation constant [37]

$$\beta_m(\omega) = \left.\frac{\partial^m \beta}{\partial \omega^m}\right|_{\omega} \tag{2.1}$$

This expression constitutes all the dispersion terms where β_0 is the phase, β_1 is the 1^{st} order dispersion, β_2 is the 2^{nd} order dispersion and β_3 is the 3^{rd} order dispersion. Higher order terms such as β_4 and β_5 also contributes to dispersion but, depending on the type of medium used for generating supercontinuum, their contribution can be included or else negligible. Its is important to note that the dispersion only affects the phase of the pulse and does not change its spectral amplitude. We now address role of each of these terms in brief.

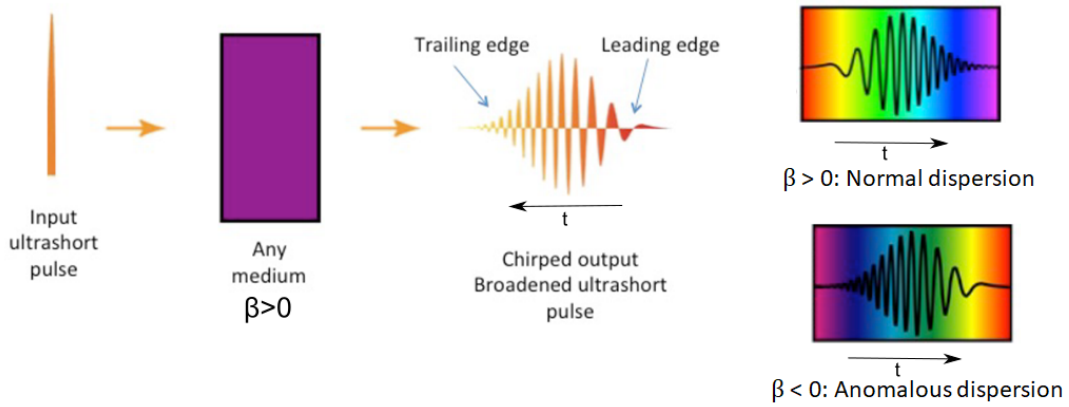

FIGURE 2.2: Illustration of an ultrafast pulse undergoing dispersion. Plots of instantaneous frequency determines the dispersion type: (a) normal dispersion and (b) anomalous dispersion.

2.1.1 Group velocity

The group velocity describes the propagation of the pulse envelope in a medium. The group velocity is defined as the inverse derivative of the propagation constant with respect to angular frequency.

$$v_g = \frac{1}{\partial\beta/\partial\omega} = \frac{1}{\beta_1(\omega)} \tag{2.2}$$

In a nonlinear interaction, the group velocity or β_1 determines the spectral overlap between the parts of the pulse in time domain. A pulse after propagating in a medium has different phase and group velocities due to chromatic dispersion. To understand the effect of phase velocity on Gaussian pulse propagation, lets assume a case where $\beta_1 < 0$. In this case the pulse envelope and the spectrum will remain the same; only the phase will shift in time. In the case of $\beta_1 > 0$, the phase shift will be positive and rest will remain the same.

2.1.2 Group velocity dispersion (GVD)

Group velocity dispersion or β_2 arises due to the frequency dependence of the group velocity. It gives insights into the relative phase or position between different spectral components of a pulse. It is given by:

$$\beta_2(\omega) = \frac{\partial^2\beta}{\partial\omega^2} \tag{2.3}$$

Often it is mentioned as the GVD parameter:

$$D = \frac{\partial\beta_1}{\partial\lambda} = \frac{\partial\beta_1}{\partial\omega}\frac{\partial\omega}{\partial\lambda} = -\frac{2\pi c}{\lambda^2}\beta_2 \tag{2.4}$$

The role of β_2 is of central importance in the supercontinuum generation process. Its primary effect is to chirp and temporally broaden the optical pulses. Further, GVD is divided into normal and anomalous dispersion regimes. In the normal dispersion regime, the GVD is positive ($\beta_2 > 0$), whereas GVD is negative ($\beta_2 < 0$) for the anomalous dispersion regime. In normal dispersion, the instantaneous frequency increases with time which implies that the red (low-frequency) components travel with higher group velocity than blue (high-frequency) components. For anomalous dispersion, the characteristic is opposite i.e. instantaneous frequency increases with time. GVD is responsible for a linear chirp, which means linear variation of instantaneous frequency. The chirp is positive when the instantaneous frequency increases with time and negative for vice versa. The spectral amplitude remains unchanged due to β_2.

2.2 Kerr nonlinearity

2.2.1 Self phase modulation

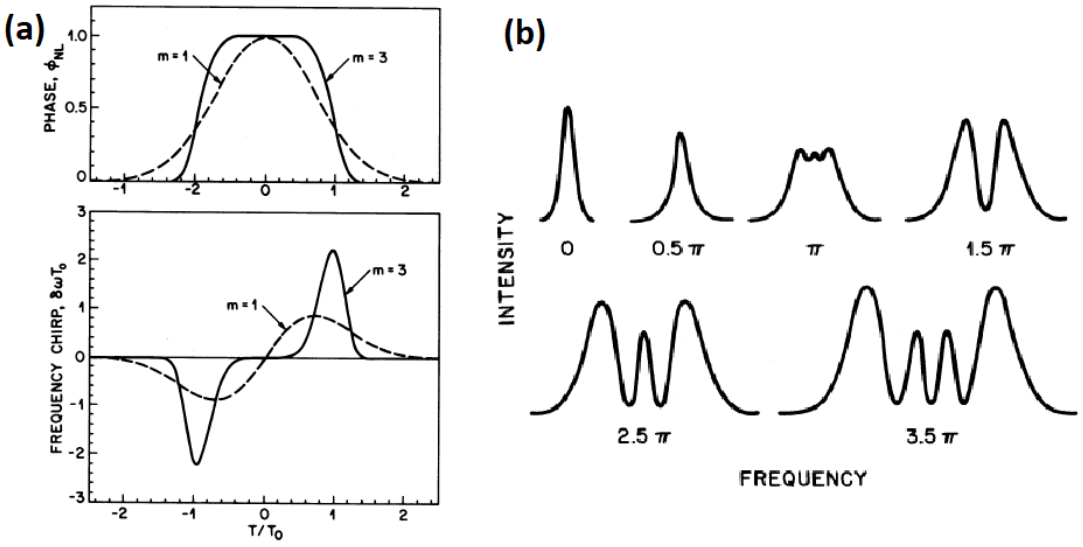

FIGURE 2.3: (a) Temporal variation of SPM induced phase shift and frequency chirp for Gaussian (dashed) and super-Gaussian pulses. Figure adapted from [37]

The most important process in supercontinuum generation in bulk materials is the Kerr effect. [38], [39]. Self-phase modulation (SPM) arises because of Kerr nonlinearity in the medium as seen in Chapter 1. The Kerr effect is a nonlinear effect occurring when an intense light beam propagates in a medium. It describes the dependence of the refractive index on the intensity.

$$n = n_0 + n_2 \cdot I \tag{2.5}$$

where n_0 is the linear and n_2 is the nonlinear refractive index. Due to third-order nonlinearities, the nonlinear refractive becomes intensity dependent. This variation of the refractive index due to the intensity leads to an effect known as self-focusing [40], [41]. It causes an increase in the refractive index in the areas where beam intensity is higher. Therefore the centre of a Gaussian beam where the intensity is high will observe a lower phase velocity. As a result, an outer propagating Gaussian beam will have a higher phase velocity than the centre causing significant curvature of the phase front. Since this action is similar to a lens, the effect is called self-focusing, which is also known as the Kerr lens. P_{crit} is the minimum power threshold required to observe the self-focusing, so that the natural divergence of the beam decreases is given by:

$$P_{crit} = \frac{3.77 \cdot \lambda^2}{8\pi \cdot n_0 \cdot n_2} \tag{2.6}$$

If the nonlinear medium is long enough, after self-focusing, the beam will collapse to a spatial soliton. This distance z_f is given by Equation (2.7) and strongly depends on the input power P and the beam waist w.

$$z_f = \frac{2.36w^2}{\lambda\sqrt{\left(\frac{P}{P_{crit}} - 0.852\right)^2 - 0.219}} \tag{2.7}$$

The interplay between self-focusing and the defocusing effects is called filamentation. If the beam is focused into the material with focusing length f, the soliton will start earlier. The total distance d after which the filamentation starts will be given by:

$$\frac{1}{d} = \frac{1}{z_f} + \frac{1}{f} \tag{2.8}$$

Self-focusing is limited by plasma defocussing or multi-photon absorption. Due to the high material density in solids, the losses are notably higher [42]. As a result, the filamentation distances lasts only a few millimetres. The advantage is that the distance is shorter due to higher nonlinear refractive index n_2. Intensity clamping is also a result of filamentation [43], [44]. As there is a stable equilibrium between self-focusing and defocusing effects, the peak intensity is extremely stable and will not exceed a maximum value else the defocusing effects dominate.

As the intensity varies in the propagation direction, the nonlinear refractive index will dominate from the Equation (2.5) and will lead to a time dependent phase given by:

$$\phi(t) = \omega_0 t - \frac{2\pi}{\lambda} z n[I(t)] \tag{2.9}$$

where, ω_0 is the central frequency of the pulse, k is the wave vector, z the propagation distance, and L the length of the nonlinear medium. As a result of changing phase in the pulse, new frequencies will be generated which is given by:

$$\omega(t) = \frac{d\phi(t)}{dt} = \omega_0 - \frac{2\pi L}{\lambda}\frac{dI(t)}{dt} n_2 \tag{2.10}$$

The Figure 2.3 illustrates the generation of new frequencies. Red frequencies will be generated on the front of the pulse where the intensity is rising, $dI(t)/dt > 0$ while on the back of the, blue frequencies will be generated as the intensity is decreasing. As a result, the generated new frequencies will be intrinsically chirped.

2.2.2 Self-steepening and shock formation

Another important nonlinear effect which is a direct consequence of self phase modulation is self-steepening. Due to intensity dependent refractive index, the group velocity v_g will also be

intensity dependent.

$$v_g = \frac{\partial \omega}{\partial k} = \frac{c}{n_0 + n_2 I - \lambda \frac{dn}{d\lambda}} \tag{2.11}$$

This implies that the centre of the pulse will have a slower group velocity. This will result in a steeper trailing edge and hence the blue side of the spectrum. This causes an asymmetry in the SPM broadened spectra of ultrashort pulses [37]. This effect is illustrated in the Figure 2.4. As the trailing edge has a very large negative gradient, the shock effect causes a large blue asymmetry to the pulse spectrum.

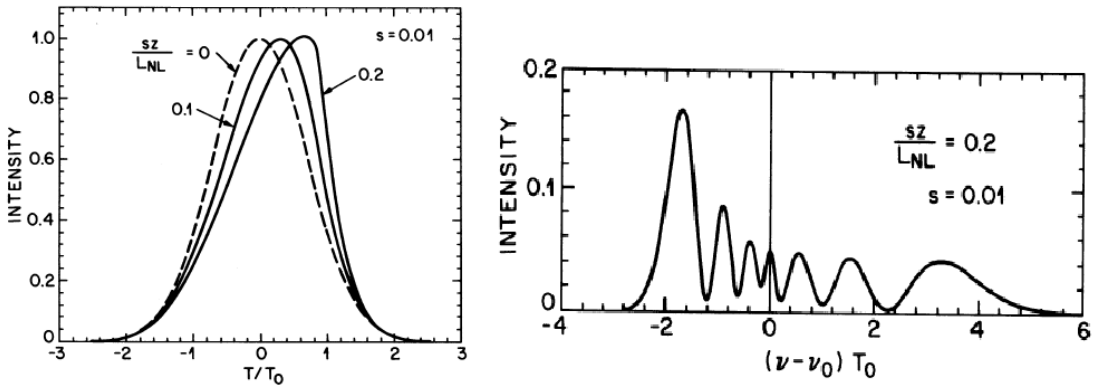

FIGURE 2.4: (a) Self steepening of Gaussian pulse in the dispersionless case. Different curve represent pulse in different time. (b) Effect of self steepening on SPM spectrum. Figure from [37]

2.3 Second-order nonlinear processes

2.3.1 Second harmonic generation

Second harmonic generation describes the process where two fundamental photons at frequency ω_1 mix to produce a single photon at frequency $\omega_3 = 2\omega_1$. The relevant nonlinear polarization contribution for the second harmonic generation is

$$\begin{aligned} P_{NL}^{(1)} &= \varepsilon_0 d_{eff} A_1^* A_2 e^i(\omega_1 - (k_2 - 2k_1)z) \\ P_{NL}^{(2)} &= \frac{\varepsilon_0 d_{eff}^*}{2} A_1^2 e^i(\omega_2 - (2k_1)z) \end{aligned} \tag{2.12}$$

where d_{eff} is a tensor based on a set of polarization components and is the sum of all the Fourier series order of the QPM gratings.

$$d_{eff}(z) = \frac{1}{2}\chi_{eff}^{(2)} \tag{2.13}$$

Now, after substituting Equation 2.12 into Equation 1.1a, and solving we get:

$$\begin{aligned} \frac{\partial A_1}{\partial z} &= -i\frac{\omega_1 d_{eff}(z)}{n_2 c} A_3 A_1^* \cdot e^{-i\Delta k_0 z} \\ \frac{\partial A_2}{\partial z} &= -i\frac{\omega_3 d_{eff}(z)^*}{n_2 c} A_1^2 \cdot e^{i\Delta k_0 z} \end{aligned} \tag{2.14}$$

where $\Delta k_0 = k_1 - 2k_2$ is the phase mismatch. Analytical solutions to the equations are given in [27], [45]. The m^{th} order associated with Fourier order of the OPM for a SHG is given by

$$\Delta k_m = k_2 - 2k_1 - mK_{QPM} \tag{2.15}$$

The order and the type of combination of fundamental and the second harmonic arises from the d_{eff} and is required for energy conservation.

2.3.2 Three wave mixing

The $\chi^{(2)}$ process involves interaction of three fields at frequency ω_p, ω_s and ω_i which are related to each other by energy conservation $\hbar\omega_p = \hbar\omega_s + \hbar\omega_i$. We will consider all three waves are co-polarised (TM) and then the nonlinear polarisation can be given as:

$$\begin{aligned} P_{NL}(\omega_p) &= 2\varepsilon_0 \chi^{(2)} E_s(\omega_s) E_i(\omega_i) \\ P_{NL}(\omega_s) &= 2\varepsilon_0 \chi^{(2)} E_p(\omega_p) E_i^*(\omega_i) \\ P_{NL}(\omega_i) &= 2\varepsilon_0 \chi^{(2)} E_p(\omega_p) E_s^*(\omega_s) \end{aligned} \tag{2.16}$$

Assuming the slowly varying envelope approximation, the three waves coupled equations that govern the parametric processes can be obtained by solving the nonlinear wave Equation [24]. The equations are:

$$\begin{aligned} \frac{\partial^2 A_p}{\partial z^2} &= -i\sigma_p A_s A_i \cdot e^{-i\Delta k z} \\ \frac{\partial^2 A_s}{\partial z^2} &= -i\sigma_s A_p A_i^* \cdot e^{-i\Delta k z} \\ \frac{\partial^2 A_i}{\partial z^2} &= -i\sigma_i A_p A_s^* \cdot e^{-i\Delta k z} \end{aligned} \tag{2.17}$$

where

$$\sigma_j = d_{eff} \cdot \frac{\omega_j}{c} \cdot n_j \; (j = p, s, i)$$

These are called the coupled-wave equations or three wave mixing. For a quasi phase matched crystal, the phase mismatch for the TWM are given by:

$$\Delta k_m = k_p - k_s - k_i - mK_{QPM} \tag{2.18}$$

2.3.3 Cascaded phase shift

The coupled wave equations outlined in the Section 2.3.2 describe efficient energy transfer between the waves provided that the phase matching condition is satisfied. The solutions of these equations vary as the phase mismatch increases. In such conditions, the waves flip each other's phase without transferring much energy between them. The resulting collective interaction closely duplicates $\chi^{(3)}$ effects such as self-phase and cross-phase modulation. This forward and backward energy transfer because of phase mismatch is called cascaded phase shift [30].

Considering a large phase mismatch in the Equation (2.14), the resulting second harmonic constitutes a rapidly varying component whose phase is changing due to a slowly varying component and the driving polarization (2.12). The rapidly varying component is $A_1^{(1)}$ and is given by:

$$A_1^{(1)} = -\frac{1}{\Delta k_0}\frac{\omega_3 d_{eff}^*}{n_2 c}A_3^2 e^{i\Delta k_0 z} \tag{2.19}$$

The more general approaches and details of this equation are given in [46]. Assuming $A_1 = A_1^{(1)}$ and using the Equation (2.14), we get,

$$\frac{dA_3}{dz} = i\frac{1}{\Delta k_0}\frac{\omega_3^2|d_{eff}|^2}{n_1 n_2 c^2}|A_3|^2 A_3 = -i\frac{3\omega_3\chi_{cascade}^{(3)}}{8n1c}|A_3|^2 A_3 \tag{2.20}$$

where $\chi_{cascade}^{(3)}$ is an effective third order susceptibility that emerges due to the cascaded $\chi^{(2)}$ effect. This gives rise to self phase modulation of the fundamental wave:

$$\chi_{cascade}^{(3)} = -\frac{1}{\Delta k_0}\frac{8\omega_3|d_{eff}|^2}{3n_2 c} \tag{2.21}$$

Chapter 3

Modelling supercontinuum generation in OPGaP

3.1 Propagation equation

Different nonlinear pulse propagation models such as carrier resolved propagation equations [47]–[52] or envelope propagation equations [53]–[57] have been used already to simulate the supercontinuum process. In this work, we use the nonlinear envelope equation (NEE) to simulate the effects of $\chi^{(3)}$ and $\chi^{(2)}$ nonlinearities in the OPGaP crystal. The NEE used in this thesis is build upon the work of Conforti and Wabnitz [58]–[60]. We start with the work of Brabec and Krausz [56], which gives us the $1+1D$ wave equation for the electric field:

$$\frac{\partial^2 \mathbf{E}(\mathbf{z},t)}{\partial \mathbf{z}^2} - \frac{1}{c^2}\frac{\partial^2}{\partial t^2}\int_{-\infty}^{+\infty} \mathbf{E}(\mathbf{z},t')\ \varepsilon(t\text{ - }t')dt' \ = \ \frac{1}{\varepsilon_0 c^2}\frac{\partial^2}{\partial t^2}\mathbf{P}_{NL}(\mathbf{z},t) \tag{3.1}$$

The equation considers the propagation of plane waves and neglects the transverse dimension. The Fourier transform ($\mathscr{F}$) and the inverse Fourier transform ($\mathscr{F}^{-1}$) are defined as:

$$\mathscr{F}\{\mathbf{E}(\omega)\} = \tilde{\mathbf{E}}(\omega) = \int_{-\infty}^{\infty} \mathbf{E}(t)e^{-i\omega t}dt$$

$$\mathscr{F}^{-1}\{\mathbf{E}(t)\} = \mathbf{E}(t) = \frac{1}{2\pi}\int_{-\infty}^{\infty} \tilde{\mathbf{E}}(\omega)e^{i\omega t}d\omega$$

Using the definition of the Fourier transform, we can write the scalar wave Equation 3.1 in the frequency domain as:

$$\frac{\partial^2 \tilde{\mathbf{E}}(\mathbf{z},\omega)}{\partial \mathbf{z}^2} + \frac{\omega^2}{c^2}\tilde{\varepsilon}(\omega)\ \tilde{\mathbf{E}}(\mathbf{z},\omega) \ = \ \frac{\omega^2}{\varepsilon_0 c^2}\tilde{\mathbf{P}}_{NL}(\mathbf{z},\omega) \tag{3.2}$$

where, c is the speed of light in vacuum, ε_0 is the dielectric permittivity, $\tilde{\chi}(\omega)$ is the linear electric susceptibility and $\tilde{\varepsilon}(\omega) = 1 + \tilde{\chi}(\omega)$. Now we write the electric field as the product of carrier wave and a slowly varying envelope, $\tilde{\mathbf{E}}(\mathbf{z},\omega) = \tilde{\mathbf{U}}(\mathbf{z},\omega)e^{-ik(\omega)z}$, where $k(\omega)$ is the propagation constant. Now, the wave equation for the new field is:

$$\frac{\partial^2\tilde{\mathbf{U}}(\mathbf{z},\omega)}{\partial\mathbf{z}^2} - 2ik(\omega)\frac{\partial\tilde{\mathbf{U}}(\mathbf{z},\omega)}{\partial\mathbf{z}} = -\frac{\omega^2}{\varepsilon_0 c^2}\tilde{\mathbf{P}}_{NL}(\mathbf{z},\omega)e^{ik(\omega)z} \tag{3.3}$$

In the above equation, the field amplitude and the phase are evolving slowly in the propagation direction z and hence we can use the slowly evolving wave approximation (SEWA) to neglect the second derivative of the field $\tilde{\mathbf{U}}$ with respect to z, and thus, we get

$$\frac{\partial\tilde{\mathbf{U}}(\mathbf{z},\omega)}{\partial\mathbf{z}} = -i\frac{\omega^2}{\varepsilon_0 c^2 k(\omega)}\tilde{\mathbf{P}}_{NL}(\mathbf{z},\omega)e^{ik(\omega)z} \tag{3.4}$$

The equation for the electric field can be obtained from the definition of $\tilde{\mathbf{U}}$.

$$\frac{\partial\tilde{\mathbf{E}}(\mathbf{z},\omega)}{\partial\mathbf{z}} + ik(\omega)\tilde{\mathbf{E}}(\mathbf{z},\omega) = -i\frac{\omega}{2\varepsilon_0 c n(\omega)}\tilde{\mathbf{P}}_{NL}(\mathbf{z},\omega) \tag{3.5}$$

The Equation 3.5 is called the forward Maxwell equation (FME) [49].

3.1.1 Definition of envelope

Electric field and its Fourier transform can be written as:

$$\mathbf{E}(\mathbf{z},t) = \frac{1}{2}\mathbf{A}(\mathbf{z},t)e^{i\omega_0 t - i\beta_0 z} + c.c. \tag{3.6}$$

$$\tilde{\mathbf{E}}(\mathbf{z},\omega) = \frac{1}{2}\mathbf{A}(\mathbf{z},\omega-\omega_0)e^{-i\beta_0 z} + c.c. \tag{3.7}$$

where, ω_0 is the carrier frequency and $\beta_0 = \Re\{k(\omega)\}$. It is critical to define the complex envelope of the field as not to put any assumptions on the frequency domain of the signal. The electric field can be analytically defined as:

$$\hat{\mathbf{E}}(\mathbf{z},t) = \mathbf{E}(\mathbf{z},t) + i\mathscr{H}\{\mathbf{E}\}(\mathbf{z},t) \tag{3.8}$$

$$\mathscr{H}\{\mathbf{E}\}(\mathbf{z},t) = \frac{1}{\pi}p.v.\int_{-\infty}^{+\infty}\frac{\mathbf{E}(\mathbf{z},t')}{t-t'}dt' \tag{3.9}$$

where $\mathscr{H}$ is the Hilbert transform of the electric field and $p.v$ represents the Cauchy principal value of the integral. The analytic signal is a signal that contains only positive frequency as it

reads:

$$\hat{\tilde{\mathbf{E}}}(\mathbf{z},\omega) \;=\; \begin{array}{ll} 2\tilde{\mathbf{E}}(\mathbf{z},\omega), & if\ \omega > 0 \\ \tilde{\mathbf{E}}(\mathbf{z},0), & if\ \omega = 0 \\ 0, & if\ \omega < 0 \end{array} \tag{3.10}$$

Due to Hermitian symmetry, only positive or negative frequencies carry information and be written as:

$$\tilde{\mathbf{E}}(\mathbf{z},\omega) \;=\; \frac{1}{2}\hat{\tilde{\mathbf{E}}}(\mathbf{z},\omega) + \frac{1}{2}\hat{\tilde{\mathbf{E}}}^{*}(\mathbf{z},-\omega) \tag{3.11}$$

And finally, we can write the complex electric field as:

$$\mathbf{A}(\mathbf{z},t) \;=\; \hat{\mathbf{E}}(\mathbf{z},t)e^{-i\omega_0 t + i\beta_0 z} \tag{3.12}$$

3.1.2 Nonlinear polarization

Following the similar steps as the electric field, the nonlinear polarization can be written as the product of complex envelope and a carrier wave and it reads

$$\mathbf{p}_{NL}(\mathbf{z},t) \;=\; \hat{\mathbf{P}}_{NL}(\mathbf{z},t)e^{-i\omega_0 t + i\beta_0 z} \tag{3.13}$$

The total nonlinear polarization can be written as the sum of quadratic and cubic nonlinearities, i.e $\mathbf{p}_{NL} \;=\; \mathbf{p}^{(2)}_{NL} + \mathbf{p}^{(3)}_{NL}$. Using the definition of the complex electric field, the quadratic $\mathbf{p}^{(2)}_{NL}$ and the cubic $\mathbf{p}^{(3)}_{NL}$ nonlinear polarization can be further expanded as

$$\begin{aligned} \mathbf{p}^{(2)}_{NL} &= \varepsilon_0\chi^{(2)}\mathbf{E}(\mathbf{z},t)^2 \\ &= \varepsilon_0\chi^{(2)}[\mathbf{A}(\mathbf{z},t)e^{-i\omega_0 t + i\beta_0 z}]^2 \\ &= \frac{\varepsilon_0\chi^{(2)}}{2}\left[2|A|^2 e^{-i\omega_0 t - + i\beta_0 z} + A^2 e^{i\omega_0 t - i\beta_0 z}\right] \\ \mathbf{p}^{(3)}_{NL} &= \varepsilon_0\chi^{(3)}\mathbf{E}(\mathbf{z},t)^3 \\ &= \varepsilon_0\chi^{(2)}[\mathbf{A}(\mathbf{z},t)e^{-i\omega_0 t + i\beta_0 z}]^3 \\ &= \frac{\varepsilon_0\chi^{(2)}}{4}\left[3|A|^2 A + A^3 e^{2i\omega_0 t + 2i\beta_0 z}\right] \end{aligned} \tag{3.14}$$

3.1.3 Nonlinear envelope equation

Substituting the expression of electric field and the Taylor series expansion of $k(\omega)$ in the Equation 3.5 yields

$$\frac{\partial(\mathbf{z},\Omega)}{\partial\mathbf{z}} + i\left[\sum_{m=1}^{\infty}\frac{i^{m+1}}{m!}\beta_m\right]\mathbf{A}(\mathbf{z},\Omega) \;=\; -i\frac{\omega}{2n(\omega)c\varepsilon_0}\tilde{p}_{NL}(\mathbf{z},\Omega) \tag{3.15}$$

where $\Omega = \omega - \omega_0$ and $\beta_m = \partial^m \beta / \partial \omega^m$. The time domain equation can be obtained by taking the inverse Fourier transform

$$\frac{\partial(\mathbf{z},t)}{\partial \mathbf{z}} + iD\mathbf{A}(\mathbf{z},t) = -i\frac{\omega}{2n_0 c\varepsilon_0}\left(1 - \frac{i}{\omega_0}\frac{\partial}{\partial t}\right) p_{NL}(\mathbf{z},t) \tag{3.16}$$

where D is the dispersion operator defined as

$$D = \left[\sum_{m=1}^{\infty} \frac{i^{m+1}}{m!}\beta_m \frac{\partial^m}{\partial t^m}\right]$$

It is convenient to write the propagating pulse in a local time frame and hence we rewrite the Equation 3.16 in a reference frame moving at group velocity β_1 (v_g) and thus by changing $\tau = t - \beta_1 z$, we get

$$\frac{\partial \mathbf{A}(\mathbf{z},\tau)}{\partial \mathbf{z}} + iD\mathbf{A}(\mathbf{z},\tau) = -i\frac{\omega_0}{2n_0 c\varepsilon_0}\left(1 - \frac{i}{\omega_0}\frac{\partial}{\partial \tau}\right) p_{NL}(\mathbf{z},\tau) \tag{3.17}$$

By changing the reference we get the NEE used in this work. Now, we substitute the total nonlinear polarization by using Equation 3.14 to get the final equation. It is important to know that the nonlinear perturbation contribution is considerably less than the linear contribution. Also, the negative frequencies are not considered as these do not phase match.

$$\begin{aligned}\frac{\partial \mathbf{A}}{\partial \mathbf{z}} + iD\mathbf{A} = i\frac{\omega_0}{2n_0 c\varepsilon_0}\left(1 - \frac{i}{\omega_0}\frac{\partial}{\partial \tau}\right) \times \\ \left\{\frac{\varepsilon_0 \chi^{(2)}}{2}\left[2|A|^2 e^{-i\omega_0\tau - i\omega_0\beta_1 z + i\beta_0 z} + A^2 e^{i\omega_0\tau + i\omega_0\beta_1 z - i\beta_0 z}\right] + \right. \\ \left. \frac{\varepsilon_0 \chi^{(3)}}{4}\left[3|A|^2 A + A^3 e^{2i\omega_0\tau + 2i\omega_0\beta_1 z - 2i\beta_0 z}\right]\right\}\end{aligned} \tag{3.18}$$

3.2 Numerical Results

3.2.1 Numerical modelling framework

Supercontinuum generation is a complex process involving many processes acting together. Therefore, to help understand the dynamics, numerical modelling can provide significant insights into these processes. However, solving the nonlinear propagation equation is challenging and complex which can also be limited by computational capabilities of system. In this section, I solve the NEE Equation 3.18 in the frequency domain using the Runge-Kutta method to show examples of full numerical modelling of the experimentally measured output spectra.

I simulate the propagation of a 90 fs long Gaussian pulse centred around 1040 nm with 1.6 MW/cm^2 peak intensity. To model the refractive index dispersion, Sellmeier coefficients were

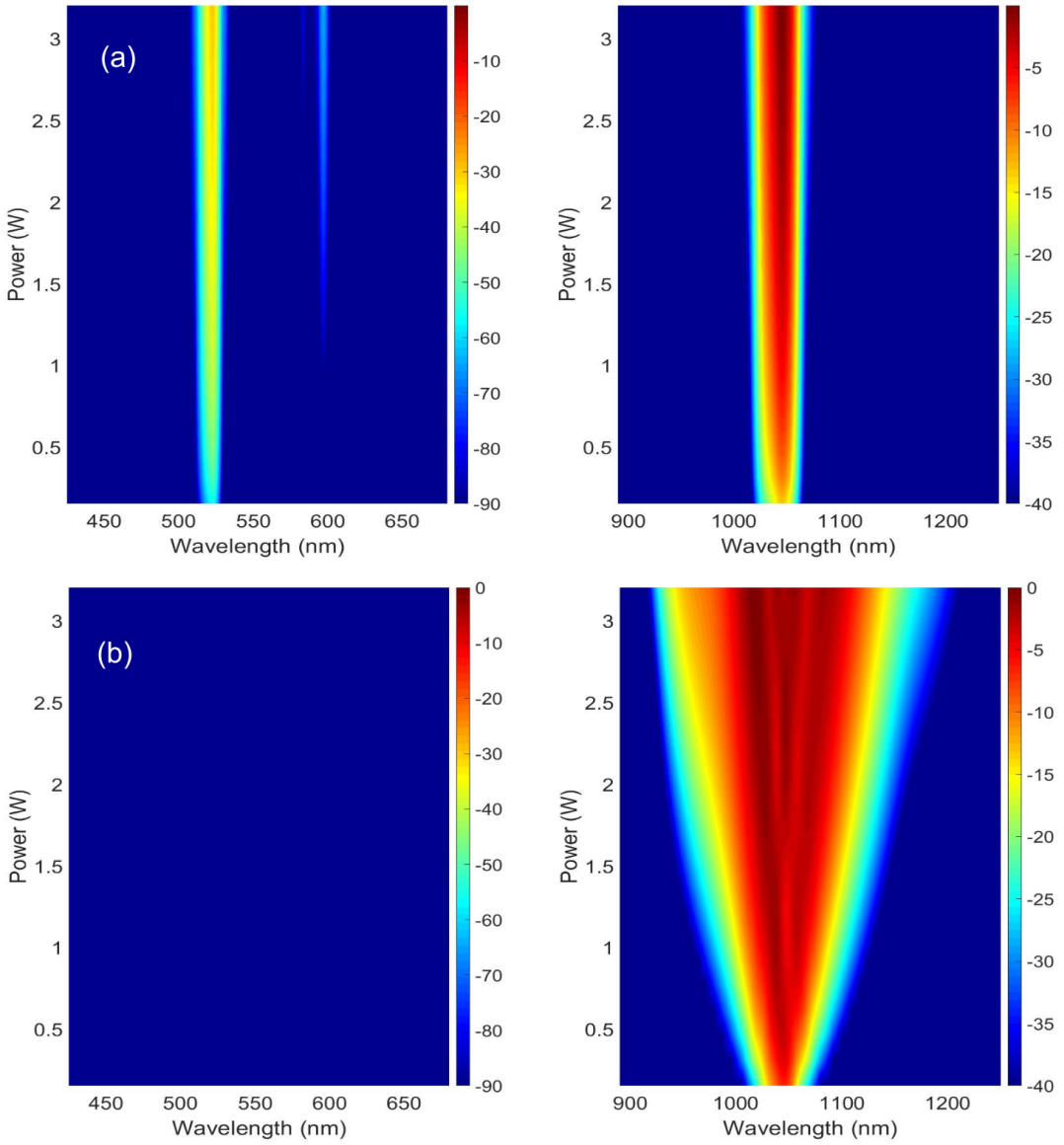

FIGURE 3.1: Simulated evolution of the visible and near-infrared spectra in 1 *mm* long and 27 μm grating period OPGaP crystal with only (a): $\chi^{(2)}$ nonlinearity active; (b): $\chi^{(3)}$ nonlinearity turned on.

inserted from the experimental data [36] with a temperature of $20^{\circ}C$. The optimum poling period was found out to be $\Lambda = 27$ μm. We used the value $\chi^{(2)}/2 = 85 \times 10^{-12}$ m/V as the second-order nonlinear coefficient and for GaP $n_2 = 6.5 \times 10^{-18}$ [61]. During experiments, two different spectrometers with filters were used to record the visible and near-infrared spectra. To mimic the experiment in the simulation, output spectra were convoluted with a visible and near-infrared filter of appropriate spectral resolution. Linear diffraction is neglected as the confocal parameter for the focal spot size is 13 *mm*. Also, spatio-temporal effects and the Raman effect are not considered.

The NEE model allows us to separately investigate the contributions from the $\chi^{(2)}$ and $\chi^{(3)}$

nonlinearities. For the initial example presented in Figure 3.1 (a), I set $\chi^{(3)} = 0$ in the NEE model to only get the contributions from second-order nonlinearity. It can be seen that there is no significant pulse broadening in the near-infrared part of the spectrum whereas we see the output at around 520 nm in the visible part of the spectrum. The green light at 520 nm is the frequency-doubled wavelength arising from the second-order nonlinearities present in the crystal in the presence of 1040 nm pump. There is little sideband generated around 600 nm which arises due to high order phase matching and parametric gain and is explained in the later subsection.

Now, to understand the effect of Kerr nonlinearity (3.1(b)),the $\chi^{(3)}$ component is retained while $\chi^{(2)}$ is set to zero in the NEE model. As a result, we see a spectral broadening in the near-infrared part of the spectrum and no second harmonic generation. The broadened sideband of the pump spectrum is due to self-phase modulation.

3.2.2 Full Model

After understanding the contributions of quadratic and cubic nonlinearities individually, we now look at an example where both $\chi^{(2)}$ and $\chi^{(3)}$ are turned on in our NEE model. Figure 3.2 shows the power spectrum obtained from the NEE model. The input narrowband pump is spectrally broadened from $950 - 1250$ *nm* due to the self-phase modulation as seen in Figure 3.1. In the visible region, we see a broadened spectrum around the second harmonic output at 520 *nm* along with some spikes.

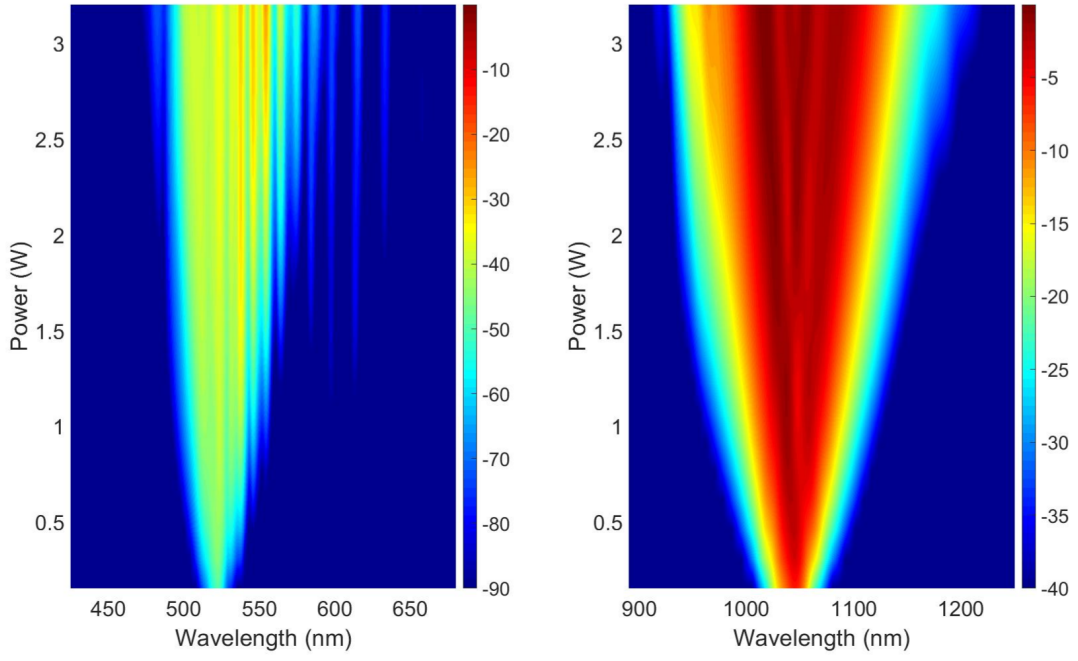

FIGURE 3.2: Simulated evolution of the visible and near-infrared spectra after propagation through a 1 *mm* long OPGaP crystal fabricated with a grating period of 27 μm.

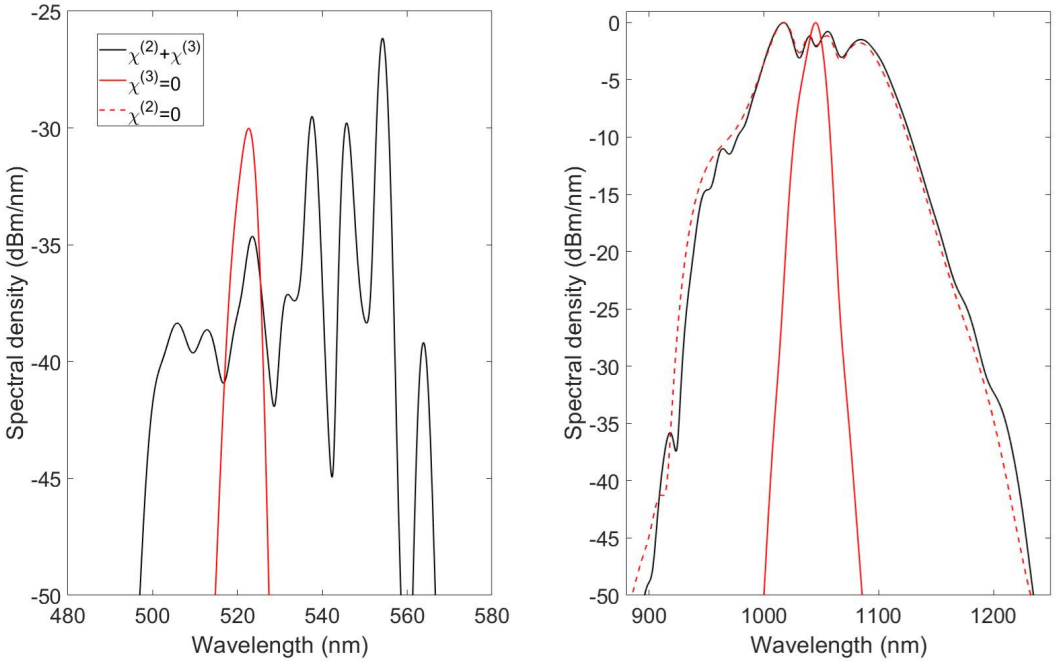

FIGURE 3.3: Comparison of simulated spectra in 1mm OPGaP with $27\mu m$ grating and the effect of switching off either quadratic or cubic nonlinearity.

Figure 3.3 shows the overlay of spectra with $\chi^{(2)}$ and $\chi^{(3)}$ acting alone and together. It can be seen that when only $\chi^{(3)}$ is turned on, the spectral broadening in the near-infrared region due to SPM is similar to the broadening when both the nonlinearities act together. This is evident as only $\chi^{(3)}$ is responsible for symmetric broadening of the pump and no light is generated in the visible reason in that case. In Figure 3.3 when we compare the visible region, one can see that the output is not the same when $\chi^{(2)}$ is acting alone. Not only the frequency-doubled content, but also some shorter and longer wavelength spikes. The origins of these spikes arise due to higher-order quasi phase matched seeded parametric gain and can be explained by considering the phasematching efficiency of OPGaP. Figure 3.4 shows the mth order difference frequency mixing in the range of 500-650 nm. We know that the 520 nm output in the visible region is generated due to frequency-doubled pump. Now, this can act as a pump to parametrically amplify longer wavelengths around 500 -650nm. As a result, it parametrically amplifies longer wavelengths around 550-600 nm. and the shorter wavelengths are amplified by the lower-order process. Hence they experience stronger conversion because of $1/m^2$ dependence of the parametric gain coefficient. This is illustrated in Figure 3.4, where a few nm pump centred at 520 nm, is shown as a dotted line which intersects many high order phasematching loci. The dotted white line intersecting the orders m =5,7,9 corresponding to the spikes around 550nm can be seen in Figure 3.3. Since the high order phase matching loci lie diagonally on the phasematching map, the spectral bandwidth of a broadband pump can be translated into the parametric signal. The above analysis assumes that some seed light already exists at wavelengths longer than 520nm. This can be explained using the frequency-doubled sidebands of the pump light. Our claim that

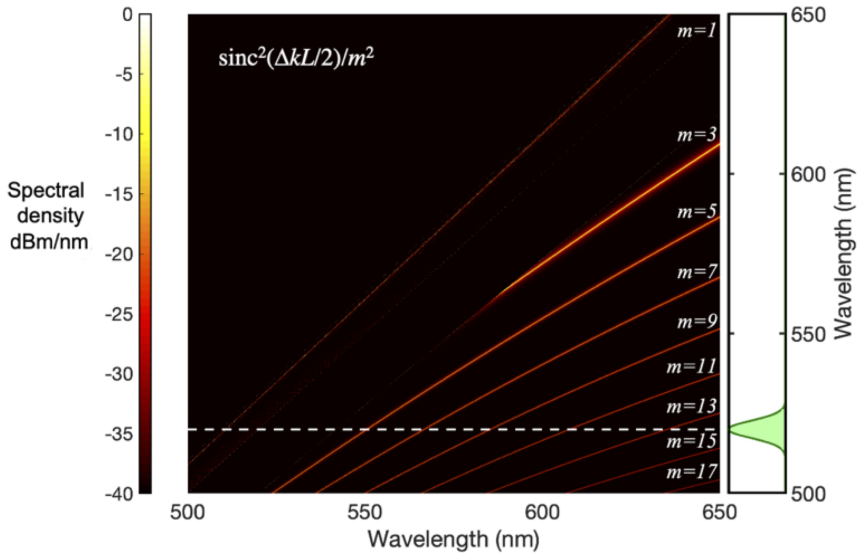

FIGURE 3.4: Fundamental and high-order $m = 3 - 17$ phasematching loci for difference-frequency mixing in a 27 period OPGaP crystal of length 1 mm. Interaction efficiency, proportional to $sinc^2(\Delta kL/2)/m^2$, is represented by the color map.

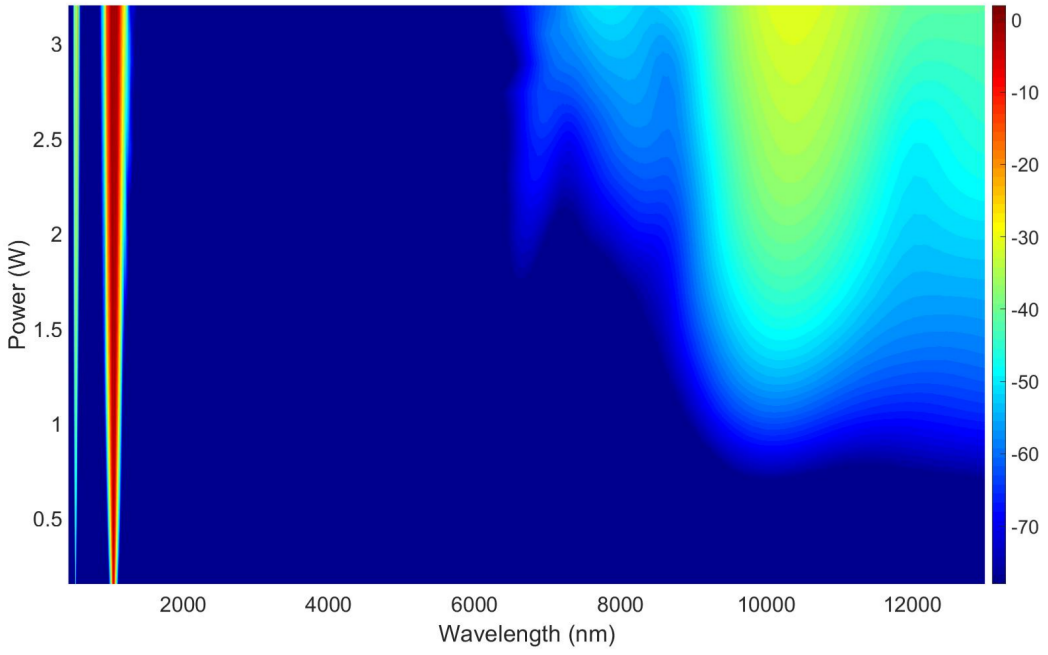

FIGURE 3.5: Full-spectrum NEE simulation, showing long-wave infrared generation above 7 μm, corresponding to idler radiation from difference frequency mixing between 520 *nm* and wavelengths shorter than 562 *nm*.

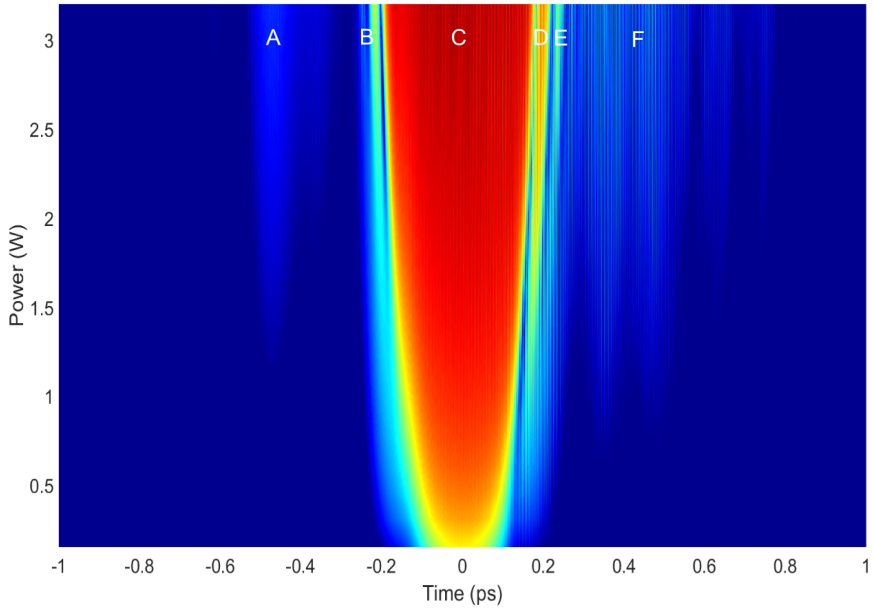

FIGURE 3.6: Pulse evolution in time domain of 1 mm OPGaP crystal with a grating period of 27 μm

parametric gain in the green is responsible for the supercontinuum generation process is further confirmed in Figure 3.5, which illustrates the long-wave infrared generation observed in the NEE model above powers where SPM broadens the spectrum to a range sufficient to generate the necessary seed wavelengths. Infrared generation occurs above 7 μm, corresponding to peak parametric gain below 562 nm.

In this work, temporal characterisation was not performed experimentally but Fig 3.6 shows the pulse evolution in the time domain. The plot shows the temporal pulse evolution as the pump power is increased. The initial pump pulse is around 100 fs and it can be seen that after exiting the pulse it broadens temporally and thus the pulse is chirped as it exits the crystal. This can be explained with the help of the spectral evolution in Figure 3.2. We can see the generation of sideband spikes after 1 W of pump power. As the sidebands in the visible region are due to cascaded a $\chi^{(2)}$ effect, the generated parametric light travels with different group velocity than the pump, and as a result we get newly generated frequencies travelling at different speeds. This can be seen in the temporal evolution as the sidebands are more prominent after 1 W of power.

To understand the temporal dynamics, let us look at each feature in Figure 3.6 individually. We suspect that the idler pulses are generated before the near-infrared sidebands and this can be seen in Figure 3.6, where the generated idler has less group velocity and is shown on the left side of the plot as label A. The label C indicates the 1040 nm pump at time t = 0. B and D point out the near-infrared sideband generation with a different group velocity. The second harmonic signal at 520 nm is shown by label E and indicates that the frequency-doubled signal is generated after the near-infrared sideband. Lastly, sidebands generated after 550 nm are shown by label

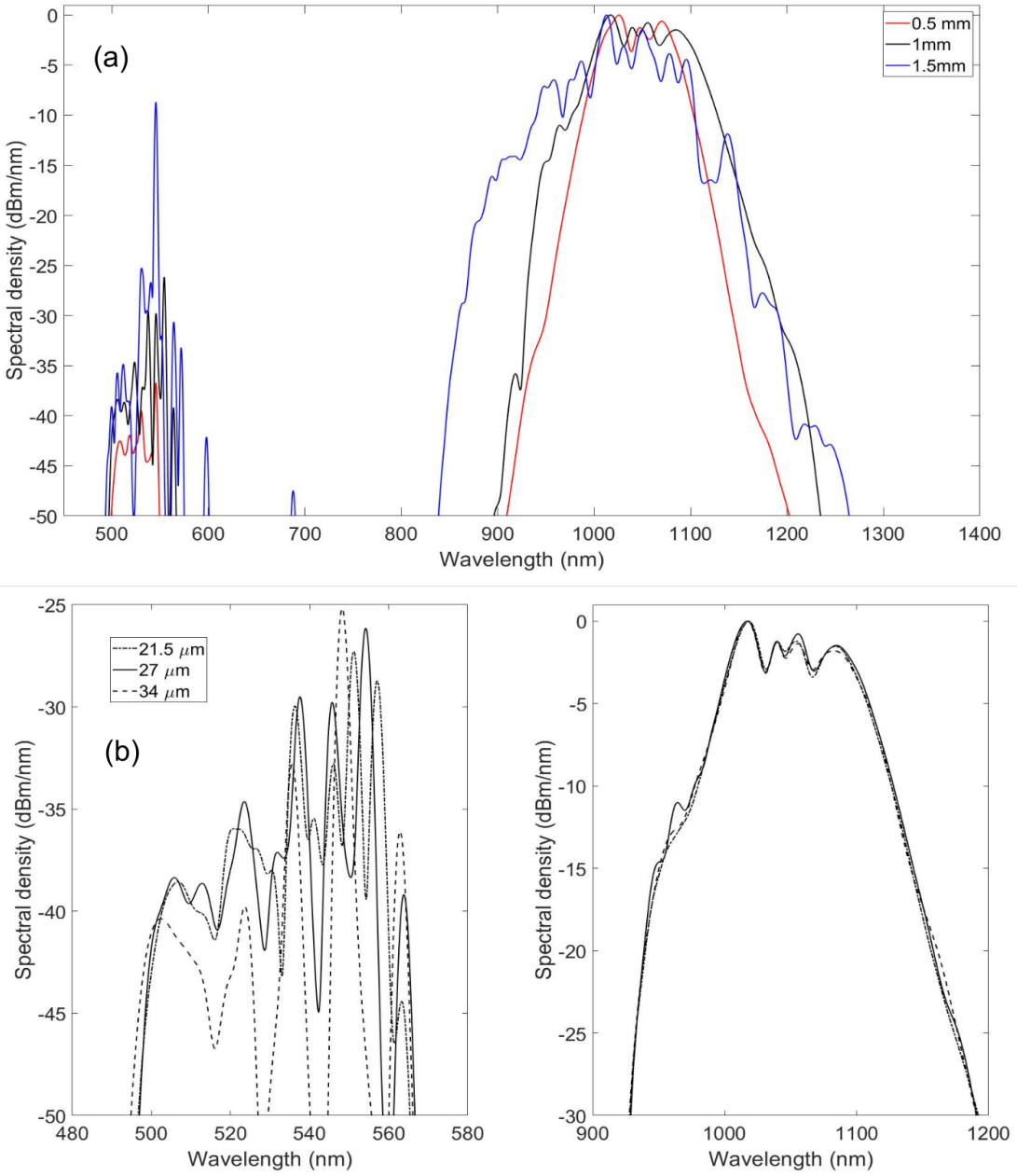

FIGURE 3.7: (a):Simulated spectra after propagating through 0.5 mm, 1 mm and 1.5 mm OPGaP crystal with a grating period of 27 μm; (b)Simulated spectra in 1mm OPGaP with different grating periods.

F. It reveals that sidebands are generated at different times and supports our cascade $\chi^{(2}$ model. Temporal cascading can be seen which confirms that each new longer wavelength green output seeds the next order amplification process. To confirm our assertion, one needs to selectively set some frequencies to zero in our model and then look at the temporal evolution. Lastly, I compare the effect of crystal length and grating period in the OPGaP crystal. In Fig 3.7 (a), a simulation of the output spectra using crystal lengths of 0.5 mm and 1.5 mm is compared with a 1 mm crystal length. Apart from the length, all other parameters are kept the same. We can see that the spectral broadening in the near-infrared region increases with an increase in crystal length

whereas, in the visible part, the spectral shape mostly remains the same except some appearance of sideband with the increase in length. The reason behind the increase in broadening with the crystal length is the self-phase modulation. Generation of new frequencies in SPM depends on the time-dependent phase which is directly proportional to the interaction length. Hence we see the broadest spectrum in the near-infrared region due to the $\chi^{(3)}$ nonlinearity. As the near-infrared spectrum is the broadest in the 1.5 mm crystal, we see parametric amplification of higher grating order and hence the appearance of new sidebands.

When the crystal grating period is varied, the near-infrared part of the spectrum remains the same but the green wavelength peaks are shifted. This is apparent as SPM induced broadening doesn't depend on the grating period while the parametric peaks are shifted. As the poling period changes, the parametric gain also shifts accordingly. This corresponds to shift in peaks in the visible part of the spectrum as it depends on the cascaded $\chi^{(2)}$ nonlinearity. This can be seen numerically in Figure. 3.7, where the output spectrum of 1 mm OPGaP with three different grating period is shown.

3.3 Conclusion

The NEE model presented here unwraps the dynamics behind the supercontinuum generation. It shows that cascaded $\chi^{(2)}$ plays an important role in the generation of supercontinuum. Due to cascaded $\chi^{(2)}$, the effective refractive index changes which induce Kerr nonlinearity and we see sidebands generated in the near-infrared part of the spectrum. This is then frequency-doubled to see the green light around 520 nm. Finally, it can be seen that due to the cascading effect, new frequencies are generated after 520nm. This is due to the parametric amplification of the sidebands. This is confirmed by looking at the high order phase matching loci and the infrared idler generation. The temporal evolution of the pulse also supports our idea of temporal cascading that new frequencies generated near the green seeds the next order process.

The 1+1D model presented here helps us to understand the fundamental process behind the supercontinuum generation but extending the model to include the Raman effects will help to investigate further. The next chapter shows the experimental results which support the qualitative findings presented in this chapter but also indicate differences in behaviour.

Chapter 4

Supercontinuum generation with a femtosecond Yb-fibre laser

4.1 Pulse characterisation using FRAC

In this work, to measure and characterise the ultrashort laser pulses, I used fringe resolved autocorrelation (FRAC). Figure 4.1 shows a schematic of the autocorrelation technique. It uses a Michelson interferometer to measure the second harmonic intensity as a function delay. The input pulse to be measured is split into two arms with same intensity using a beam splitter. On one of the arms, a delay line is set to change the temporal overlap between both the pulse. The reflected pulses from both arms coherently combine in the beam splitter and are sent to the detector. As a result, interference fringes occur with respect to the delay. The FRAC signal is given by:

$$\begin{aligned} I_{FRAC}(\tau) &= \int_{-\infty}^{\infty} |[E(t)+E(t-\tau)]^2|^2 dt \\ &= \int_{-\infty}^{\infty} |E(t)^2+2E(t)E(t-\tau)+E(t-\tau)^2|^2 dt \end{aligned} \tag{4.1}$$

By expanding further, we get

$$\begin{aligned} I_{FRAC}(\tau) &= \int_{-\infty}^{\infty} I(t)^2+I(t-\tau)^2 dt \\ &+ \int_{-\infty}^{\infty} I(t)+I(t-\tau) ReE(t)E*(t-\tau) dt \\ &+ \int_{-\infty}^{\infty} ReE(t)^2 E*(t-\tau)^2 dt \\ &+ \int_{-\infty}^{\infty} I(t)I(t-\tau) dt \end{aligned} \tag{4.2}$$

Thus, the FRAC signal contains a constant term, the interferograms of the input pulse, its second harmonic and the intensity autocorrelation. The intensity autocorrelation term which we read

from the oscilloscope is given by:

$$I_{IAC}(\tau) = \int_{-\infty}^{\infty} I(t)I(t-\tau)dt \tag{4.3}$$

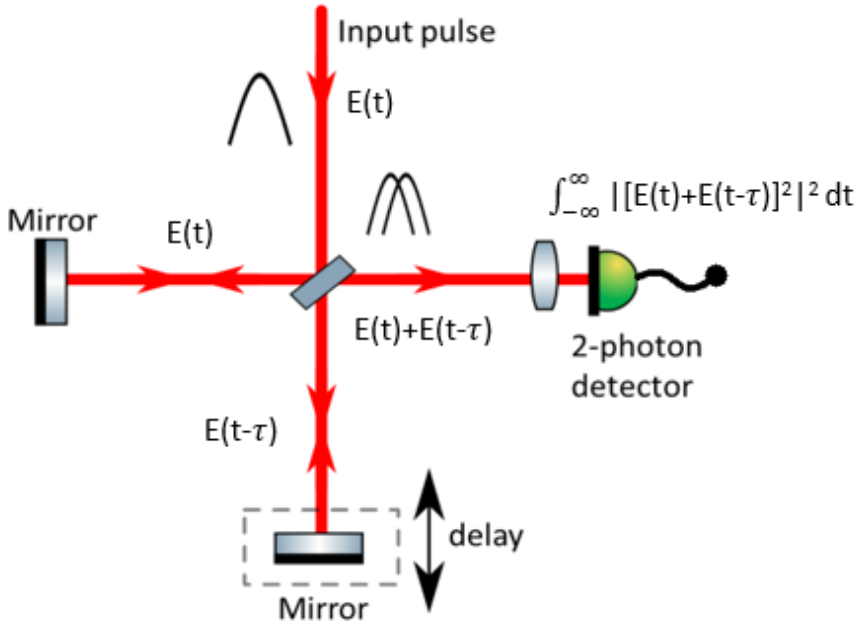

FIGURE 4.1: Illustration of the Michelson based fringe resolved autocorrelation (FRAC) technique.

4.2 Experimental methods

In our setup, a speaker is used as a delay line and a high speed GaAsP photodetector is used instead of second harmonic crystal. The autocorrelation signal is generated due to 2 photon absorption in the GaAsP detector. The signal from the photodetector is recorded by Tiepie Handyscope HS6 DIFF USB oscilloscope. The pulse duration we get from the raw autocorrealtion signal is called the intensity autocorrelation function. To get actual temporal width of the pulses, we have to multiply it by a deconvolution factor. For Gaussian pulses this factor is 0.707. Fig 4.2 (a) shows the raw autocorrelation signal with temporal duration as 166 fs. The actual pulse duration ($\Delta\tau_{FWHM}$) after deconvolution was found out to be 118 fs.

The pump laser was a commercial Yb:fibre laser from Chromacity which delivered 1040nm uncompressed pulses. Figure 4.2 (b) shows the output spectrum of the laser. The maximum average power output of the laser was 3.5 W at a 100 MHz repetition rate. The pulses directly emitted from the laser were uncompressed and too long for generating the supercontinuum and

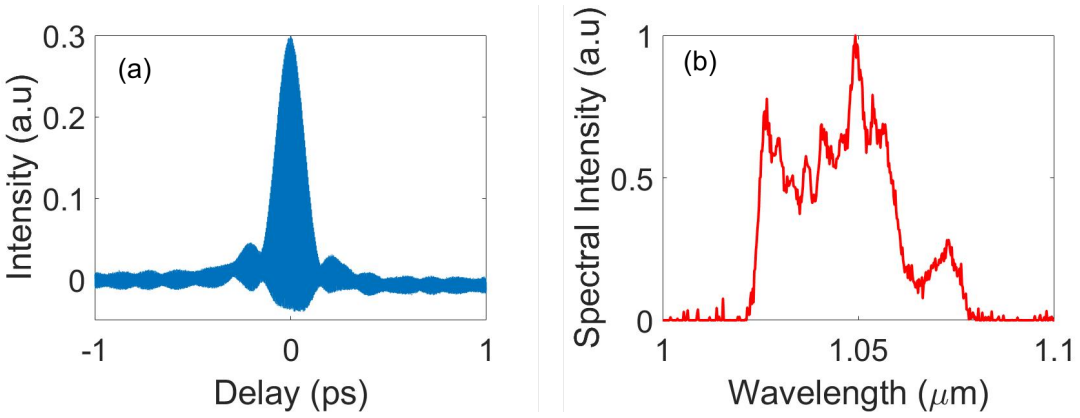

FIGURE 4.2: (a): Autocorrelation trace of the laser showing nearly compressed pulses at $\Delta\tau_{FWHM}$=118 fs. (b): Laser spectrum centered at 1040nm.

so were compressed to 90 fs using a transmission grating pair. Then the compressed pulse is focused down to a 25 μm radius spot into the 1mm OPGaP crystal. The experiment was carried out in a single pass configuration. The output spectra were recorded using a visible spectrometer (Ocean Optics QEPro) to cover 400–900 nm and an optical spectrum analyzer (Ando AQ6317B) for near-infrared wavelengths.

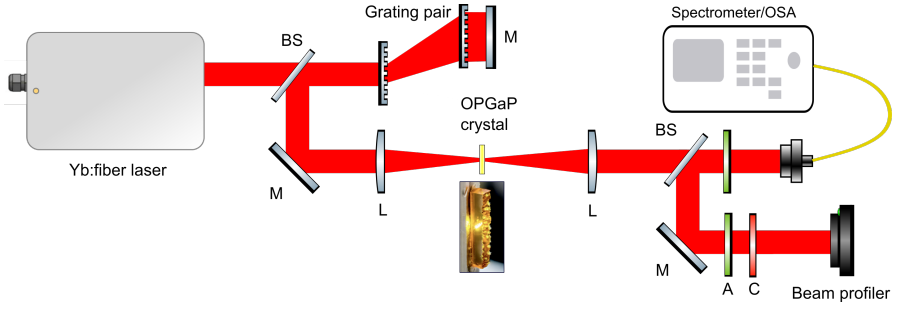

FIGURE 4.3: Supercontinuum generation setup. The resulting supercontinuum was measured using a visible spectrometer and optical spectrum analyzer (OSA), and also with a beam profiling camera. BS - beam splitter; M-mirror; L-lens; A-attenuator; C- color filter.

4.3 Experimental results

To examine the beam quality and the structure of supercontinuum components, its spatial distribution was recorded with a Thorlabs beam profiling camera (BC106N-VIS/M). To isolate the wavelengths, different colour filters were used to record the beam profiles at different wavelengths. Figure 4.4 shows the beam size at different wavelengths. The pump was measured at low power and a bandpass filter was used to measure beam at 450-650 nm wavelengths. To measure the second harmonic at 520 nm, a $\pm$10nm bandpass filter was used. High and low pass

filters were used to capture the beam at long and short wavelengths respectively. As comparison of the relative beam sizes was not possible due to the varying profiling camera positions necessitated by the different filtering arrangements used.

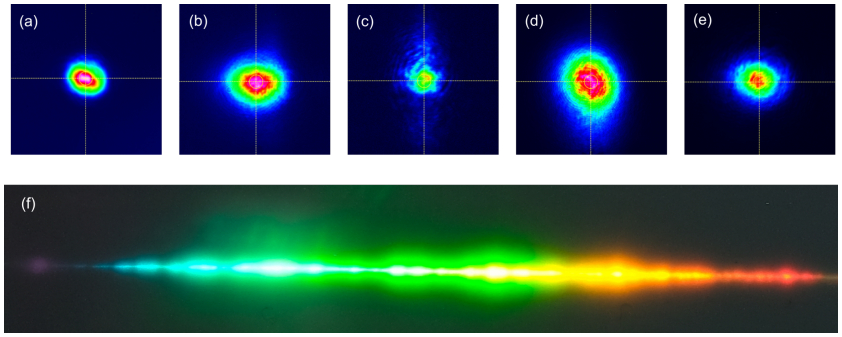

FIGURE 4.4: Beam profile of (a) pump light at 1040 nm; (b) all visible outputs; (c) wavelengths <500 nm; (d) wavelengths at 520 nm ±10 nm; and (e) wavelengths >600 nm. Profiles were measured at different observation planes, so their relative sizes are not comparable.(f) Visible supercontinuum output as seen after dispersing through a prism.

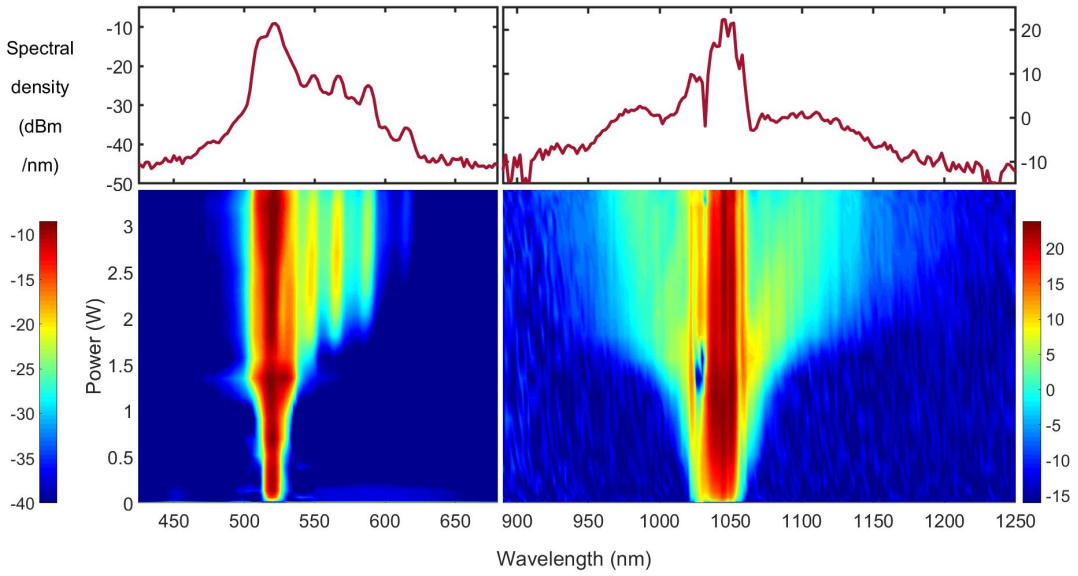

FIGURE 4.5: Upper panels: output spectra at maximum pump power, recorded using a visible spectrometer and an optical spectrum analyzer. Lower panels: evolution of the supercontinuum for average pump powers from zero to 3.2 W.

The output spectrum and evolution of the supercontinuum is shown in Figure 4.5. The evolution presented was measured by linearly increasing the pump power to a maximum of 3.2W which corresponded to an intensity of around 20 GW/cm^2. At the highest pump intensity, the spectral broadening extends from 450-600nm in the visible region and 950-1250nm in the near-infrared region. The broad visible coverage can be readily seen from the photograph in Figure 4.4 (f), which was recorded after dispersing the visible components of the spectrum using a diffraction grating and imaging the spectrum with a lens. As seen in the numerical simulations in Chapter

3, here we can also observe the spectral broadening due to self-phase modulation in the near-infrared region. There is a strong signal generated at 520 nm indicating the generation of the second harmonic of the pump. In Figure 4.5 the higher-order sidebands $m = 7, 9, 11$ can be seen near the frequency-doubled signal. Side-bands present near the frequency-doubled spectra confirm our model of high order quasi-phasematched parametric amplification.

4.4 Discussion and comparison with the numerical results

In Figure 4.5, the shorter wavelengths are amplified by lower-order processes and hence they experience stronger conversion because of the $1/m^2$ dependence of the parametric gain coefficient. Whereas, the high-order phasematching loci occupy narrow bands as they lie diagonally on the phasematching map resulting in a transfer of pump wavelength into the parametric signal wavelength. Good agreement is seen in the first few peaks in Figure 4.5 in the visible region when compared with numerical results in Figure 3.2. Peaks corresponding to m = 5,7 and 9 in Figure 3.4 match well with the experimental result but higher-order peaks agree less well. This is evident as small errors in the refractive index data used for calculation are amplified by a factor of m and can result in dramatic changes to the phasematching loci. This is illustrated in Figure 4.6 where experimental data are superimposed with numerical simulation to show the high higher-order peaks resulting from OPGaP phase matching loci.

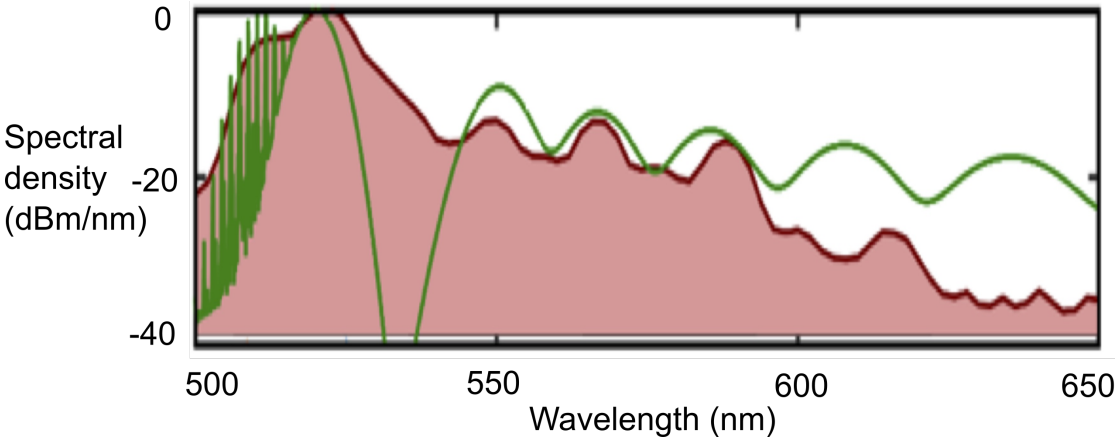

FIGURE 4.6: Green indicates the narrow 520 nm pump spectrum is mapped into multiple signal pulses and the red shaded plot shows the experimentally measured spectrum

The fundamental broadening into the near-infrared sidebands due to the Kerr nonlinearity is evident in the numerical simulations 3.2 but experimental supercontinuum spectral distribution shows less broadening in Figure 4.5. This means that for some reason we see a stronger SPM in the numerical results than observed in experiments. The weaker SPM in the experiment can be explained with the help of Figure 4.7. It shows the x and y beam profile data collected after the OPGaP crystal at the minimum and maximum powers. A power-dependent defocusing

effect can be observed at high pump powers. This can be seen in the evolution where the beam starts to diverge with an increase in pump power. A power-dependent defocusing effect cannot be easily explained by either self-focusing or thermal lensing, as in GaP both would imply positive lensing and would result in a tighter focus and stronger SPM than we experimentally observe. Instead, we attribute the weaker SPM to self-defocusing of the fundamental beam due to cascaded second-order effects [62].

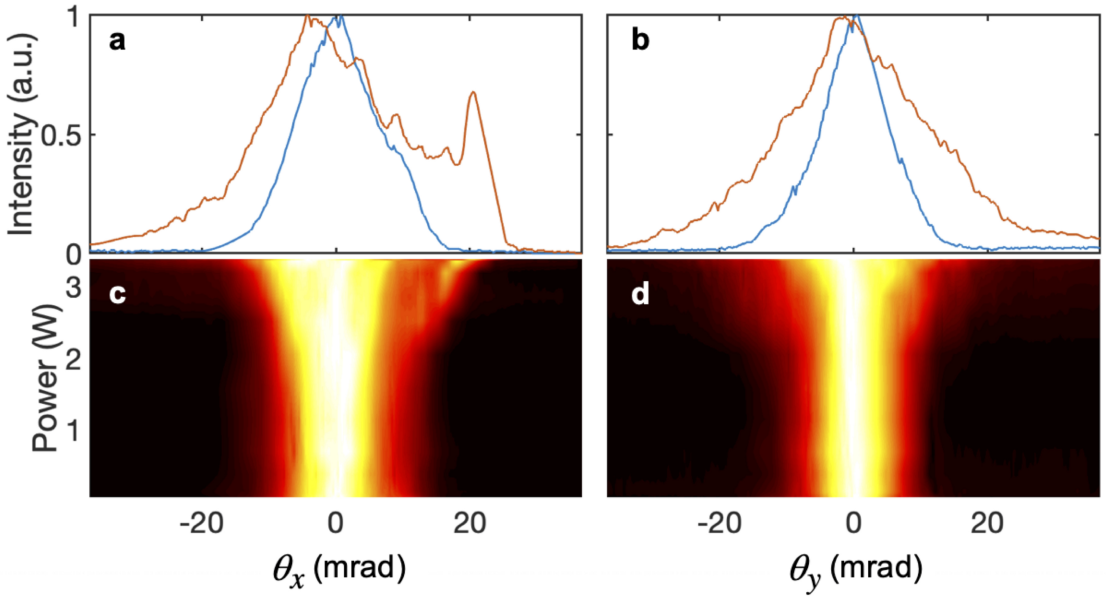

FIGURE 4.7: Profiles of the fundamental beam after the OPGaP crystal, showing a power-dependent self-defocusing effect, which we attribute to cascaded second-order effects. Panels (a) and (b) show, respectively, the x and y beam profiles at minimum (blue) and maximum (red) powers. The corresponding color maps show the beam intensity on a linear scale, indicating a divergence that approximately doubles as the power is increased from 60mW to 3.38W

The result presented in [63] shows that $\chi^{(2)}(\omega;2\omega,-\omega):\chi^{(2)}(2\omega;\omega,\omega)$ cascading causes the fundamental beam to experience a peak nonlinearity phase shift of -19 rad. This corresponds to $n_2^{eff} \approx -6.2\times10^{-13}cm^2/W$ which is opposite in sign and nearly 10 times larger than Kerr $n_2 = 6.5\times10^{-14}cm^2/W$. This explains the nature of strong defocusing in the beam profile data. Hence, strong negative defocusing is associated with this nonlinearity leads to a self-limiting behavior that weakens further SPM driven broadening. To further understand the full dynamics of the supercontinuum process, additional effects such as thermal, cascaded $\chi^{(2)}$, and even photorefractive effects [64], [65] would need to be included, but modelling accuracy would ultimately be limited by uncertainties in the experimental and material parameters, e.g., grating nonuniformity.

Chapter 5

Conclusions and outlook

In this thesis, using nanojoule-level pulses from a high-repetition-rate femtosecond oscillators, I have demonstrated a new form of supercontinuum generation in a quasi-phasematched OPGaP crystal. Numerical modelling matches suitably enough to explain the demonstrated results. The results and analysis explain the origin of the supercontinuum due to a cascaded process.

In Chapter 3, I present a NEE model to explain the supercontinuum process. The model is built upon the framework of the 1+1D propagation equation and uses the forward Maxwell's equation to get the generated output field. The simulation results tell us that the nonlinear broadening caused in the near-infrared region of the spectrum is due to the cubic nonlinearity. Broadening in the visible part is due to frequency-doubled signal which acts as a seed and parametrically amplify the weak SPM sideband while simultaneously generating long-wavelength idler. This assertion is also confirmed in the time-domain evolution of the spectrum and the results are discussed in the section.

In Chapter 4, I reported the experimental demonstration of a supercontinuum in OPGaP using 32-nJ femtosecond pulses. The generated supercontinuum showed an overall similar shape and agreed well with the simulation except it showed less spectral broadening in the near-infrared part. In the experiment, the $\chi^{(3)}$ nonlinearity was weaker when compared with the simulation. This discrepancy arises due to a strong negative defocusing effect which can be seen from the beam profile plots. The power-dependent defocusing effect observed is attributed to cascaded second-order effects in the OPGaP crystal, and it serves to self-limit the amount of SPM-induced spectral broadening in the crystal.

In conclusion, our NEE model works well to unwrap the dynamics behind the generated supercontinuum but fails to incorporate the spatial dynamics associated with a power-dependent negative n_2 nonlinear refractive index. More detailed analysis needs to be done in order to understand the dynamics with precision. By incorporating the Raman effects and defocusing effects,

more realistic analysis can be obtained. With the ready possibility of using engineered quasi-phasematching to enhance the high-order effects responsible for supercontinuum generation, it may be possible to reduce the average power needed to levels where greater spectral broadening is achieved along with reduced parasitic effects.

Appendix A

Publication

optica

Supercontinuum generation in orientation-patterned gallium phosphide

Marius Rutkauskas, Anchit Srivastava, and Derryck T. Reid*

Scottish Universities Physics Alliance (SUPA), Institute of Photonics and Quantum Sciences, School of Engineering and Physical Sciences, Heriot–Watt University, Edinburgh EH14 4AS, UK
**Corresponding author: D.T.Reid@hw.ac.uk*

Received 5 December 2019; revised 13 January 2020; accepted 13 January 2020 (Doc. ID 385200); published 13 February 2020

Supercontinuum generation from nanojoule femtosecond lasers is well known in photonic-crystal fibers, channel waveguides, and micro-resonators, in which strong confinement shapes their dispersion and provides sufficient intensity for self-phase modulation, four-wave mixing, and Raman scattering to cause substantial spectral broadening. Until now, supercontinuum generation in bulk media has not been observed at equivalent energies, but here we introduce a new mechanism combining second- and third-order nonlinearities to produce broadband visible light in orientation-patterned gallium phosphide. A supercontinuum from the blue/green to the red is produced from 32 nJ 1040 nm femtosecond pulses, and a nonlinear-envelope-equation model including $\chi^{(2)}$ and $\chi^{(3)}$ nonlinearities implies that high-order parametric gain pumped by the second-harmonic light of the laser and seeded by self-phase-modulated sidebands is responsible.

https://doi.org/10.1364/OPTICA.385200

Quasi-phase-matching [1] makes it possible even for high-order nonlinear processes in $\chi^{(2)}$ materials to access substantial effective nonlinear coefficients. Early work in periodically poled lithium niobate (PPLN) demonstrated that this facility, when combined with the high intensities available within guided-wave devices, enabled a form of supercontinuum generation that exploited multiple cascaded and high-order three-wave interactions to generate supercontinua [2]. This approach has since been refined both theoretically [3] and experimentally [4] to deliver greater control of such processes, but it has remained limited to waveguide devices, and principally to the material lithium niobate. Engineerable phase matching in semiconductors like orientation-patterned gallium arsenide (OPGaAs) [5] and orientation-patterned gallium phosphide (OPGaP) [6] has enabled the demonstration of highly efficient ultra-broadband or extremely tunable femtosecond optical parametric oscillators [7,8]. In particular, OPGaP combines transparency extending well into the visible region with a high nonlinear coefficient ($d_{14} = 70.6\ \mathrm{pm\ V^{-1}}$) [9] that results in a nonlinear figure of merit (d_{eff}^2/n^3) 3 times that of PPLN [9]. When such a high nonlinear coupling is available along with a strong driving field, many high-order processes become relatively efficient in quasi-phase-matched media; for example, the first report of optical parametric oscillation in OPGaP observed ninth-order visible light generation using narrow-linewidth nanosecond pump pulses [9].

Here we report broadband supercontinuum generation in OPGaP pumped by 1040 nm pulses from a sub-100 fs Yb:fiber laser operating at 100 MHz (Chromacity 1040). As illustrated in Fig. 1, the pulses are tightly focused into a 27 μm period crystal of length 1 mm, achieving intensities in excess of 20 GW cm^{-2} in the crystal. Spectra were recorded using a visible spectrometer (Ocean Optics QEPro) to cover 400–900 nm and an optical spectrum analyzer (Ando AQ6317B) for longer wavelengths. Various reflective and transmissive color filters were used to isolate wavebands near 1040 nm (pump, measured at low power), 450–650 nm (all visible outputs), < 500 nm (blue/green supercontinuum), near 520 nm [pump second-harmonic generation (SHG) and green supercontinuum], and > 600 nm (red supercontinuum), allowing their spatial distributions to be recorded with a beam profiling camera. The purpose of these measurements was to examine the beam quality and structure of the supercontinuum components; comparison of the relative beam sizes in Fig. 1 is not possible due to the varying profiling camera positions necessitated by the different filtering arrangements used.

The evolution of the supercontinuum spectrum is presented in Fig. 2(a) for average pump powers increasing linearly to 3.2 W, corresponding to an intensity of around 20 GW cm^{-2}. At the highest pump intensity, the spectral coverage extends from the blue/green to the red, from approximately 450–600 nm, and then in the infrared from 950–1250 nm. The broad visible coverage can be readily seen from the photograph in Fig. 2(b), which was recorded after dispersing the visible components of the spectrum using a diffraction grating and imaging the spectrum with a lens. The generation is only observed when the pump pulses, which are produced by an Yb:fiber master-oscillator power-amplifier system, are fully compressed to their minimum durations of around 100 fs.

The fundamental origin of the supercontinuum generation can be understood by considering the main image of Fig. 3, which presents the phase-matching efficiency map $\mathrm{sinc}^2(\Delta kL/2)/m^2$ for mth-order difference-frequency mixing between wavelengths in the range 500–650 nm. It shows that the second harmonic of the laser at 520 nm (marked as the white dashed line on Fig. 3)

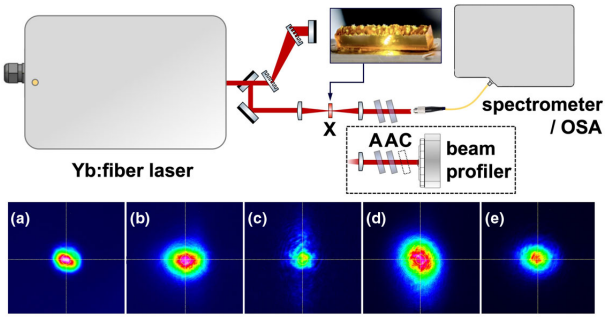

Fig. 1. Supercontinuum generation experiment. Stretched pulses from an Yb:fiber laser were de-chirped in a grating compressor before being focused into an OPGaP crystal (X). The resulting supercontinuum was measured using a visible spectrometer and optical spectrum analyzer (OSA), and also with a beam profiling camera. Intense pump light was rejected using two attenuators (A), and beam profiling employed different color filters (C) to isolate: (a) pump light at 1040 nm; (b) all visible outputs; (c) wavelengths < 500 nm; (d) wavelengths at 520 nm±10 nm; and (e) wavelengths > 600 nm. Profiles were measured at different observation planes, so their relative sizes are not comparable.

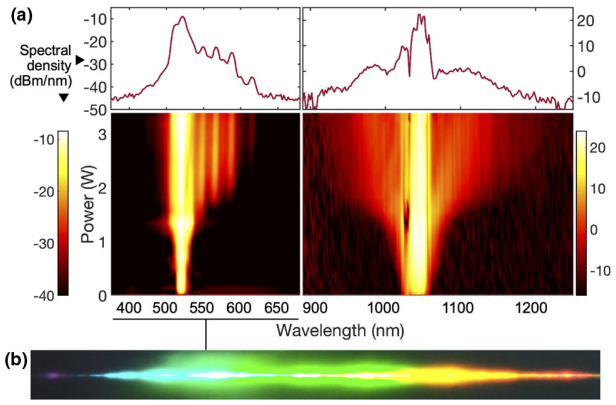

Fig. 2. (a) Upper panels: output spectra at maximum pump power, recorded using a visible spectrometer and an optical spectrum analyzer. Lower panels: evolution of the supercontinuum for average pump powers from zero to 3.2 W. (b) Photograph of the visible output corresponding to approximately 450–600 nm. A weak violet color is visible at the short-wavelength edge of the image.

can act as a pump to parametrically amplify neighboring longer wavelengths from around 550–600 nm. Shorter wavelengths are amplified by lower-order processes than higher wavelengths, and so they experience stronger conversion because of the $1/m^2$ dependence of the parametric gain coefficient. While the high-order phase-matching loci occupy very narrow bands, they lie diagonally on the phase-matching map, which means that the spectral bandwidth of a broadband pump wave can be translated into the parametric signal wavelength. To illustrate this, the right panel of Fig. 3 shows the spectrum of a few-nanometer (nm)-wide 520 nm pump wave, whose product with the phase-matching map is shown in the top panel of Fig. 3 and compared with the experimental supercontinuum. Good agreement is seen in the positions of the first few peaks, corresponding to $m = 5$, 7, and 9. The positions of the higher-order peaks agree less well, but this is not surprising since even tiny errors in the refractive index data used for the calculation [10] are amplified by a factor of m and can result in noticeable changes to the phase-matching loci.

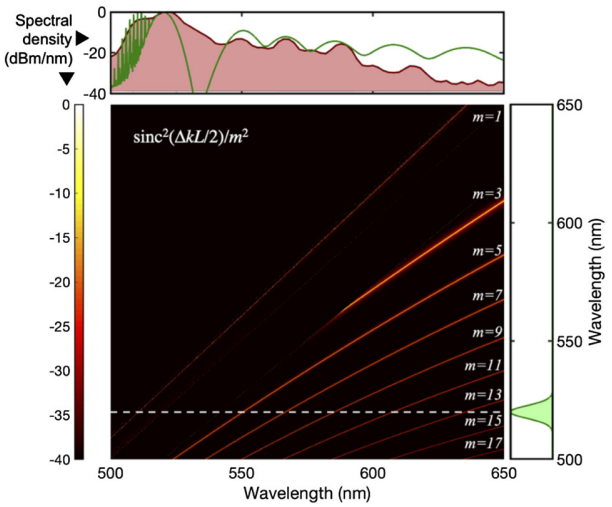

Fig. 3. Fundamental and high-order ($m = 3 - 17$) phase-matching loci for difference-frequency mixing in a 27 μm period OPGaP crystal of length 1 mm. Interaction efficiency, proportional to $\mathrm{sinc}^2(\Delta kL/2)/m^2$, is represented by the color map. Strong second-harmonic light centered at 520 nm (dashed line) acts as a pump to amplify neighboring longer wavelengths that satisfy a high-order phase-matching condition. The bandwidth of the 520 nm pump pulses is transferred into these signal pulses, which have sufficient spectral width to form a supercontinuum. This process is illustrated by considering how a narrow 520 nm pump spectrum (right axis) is mapped into multiple signal pulses (top axis, green). For comparison, the top axis shows in red the experimentally measured spectrum, whose maxima agree well with those predicted for $m = 5$, 7, and 9. At higher values of m, the experimental and calculated behaviors are more sensitive to uncertainties in the OPGaP fabrication and in the Sellmeier equations, leading to differences in the positions of the conversion maxima.

The above analysis assumes that some seed light already exists at wavelengths longer than 520 nm. By using a numerical simulation to solve a combined $\chi^{(2)}$ and $\chi^{(3)}$ nonlinear envelope equation (NEE), we show that frequency-doubled self-phase modulation (SPM) sidebands of the pump light are the origin of this seed light. Our NEE model provides a rigorous means of analyzing ultra-broadband pulse evolution in a medium possessing both an engineered $\chi^{(2)}$ nonlinearity in the form of a quasi-phase-matched grating and an intrinsic $\chi^{(3)}$ nonlinearity. Unlike the coupled-wave equations, such an approach makes no prior assumptions about the number of interacting fields or the processes involved. A similar method has already been successfully applied to predict the structure of an octave-spanning supercontinuum generated in a PPLN waveguide [3,4].

The intra-crystal focus has a Rayleigh range of 6.5 mm at 1040 nm, meaning that linear diffraction is insignificant over the crystal length of 1 mm, so our approach follows the 1 + 1D formalism in [11–15], which leads to a NEE with the form

$$\frac{\partial A}{\partial z} + iDA = -i\frac{\omega_o}{2n_o c\varepsilon_o}\left(1 - \frac{i}{\omega_o}\frac{\partial}{\partial \tau}\right)$$

$$\times \left(\frac{\varepsilon_o \chi^{(2)}}{2}\left[A^2 e^{i\omega_o \tau + i\omega_o \beta_1 z - i\beta_o z} + 2|A|^2 e^{-i\omega_o \tau - i\omega_o \beta_1 z + i\beta_o z}\right]\right.$$

$$\left. + \frac{\varepsilon_o \chi^{(3)}}{4}\left[3|A|^2 A + A^3 e^{2i\omega_o \tau + i2\omega_o \beta_1 z - 2i\beta_o z}\right]\right),$$

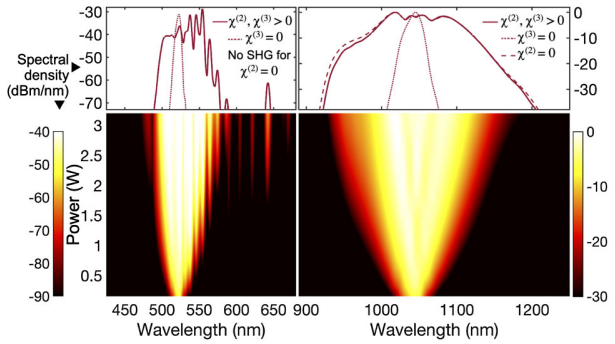

Fig. 4. Simulated evolution of the visible and near-infrared spectra after propagation through a 1 mm long OPGaP crystal fabricated with a grating period of 27 μm. The upper panels show the spectra obtained at maximum pump power (3.2 W) and the effect on these of switching off either the $\chi^{(2)}$ or $\chi^{(3)}$ nonlinearity.

where $\tau = t - \beta_1 z$ is the coordinate system moving at the reference group velocity, and the dispersion operator is given by

$$D = \sum_{n=2}^{n=\infty} \frac{i^{n+1}}{n!} \beta_n \frac{\partial^n}{\partial t^n}.$$

The refractive index of GaP was taken from a new temperature-dependent Sellmeier equation [10], which has validity from 700 nm to 12.5 μm and was expected to provide more accurate short-wavelength values than the more commonly used expression in [16]. Wavelength-dependent linear absorption at wavelengths close to the band edge was included using data from [17]. Using the NEE and data for $\chi^{(2)}$ and $\chi^{(3)}$ in OPGaP from [9] and [18], respectively, we modeled the supercontinuum generation, taking as the input a transform-limited pulse with a spectrum matching that measured experimentally at 1040 nm. We then normalized the pulse peak power so that the energy matched the experimental values and calculated the intensity according to the experimental focal-spot radius of 25 μm. The confocal parameter for this focal spot size is 13 mm, so linear diffraction can be neglected; however, spatio-temporal effects are not included in the model but do manifest themselves experimentally, as explained later.

In Fig. 4 we present the propagation modeling results for a 27 μm OPGaP grating. Powers are chosen to match the range examined experimentally in Fig. 2. Using the NEE model allows us to separately investigate the contributions from the $\chi^{(2)}$ and $\chi^{(3)}$ nonlinearities. The color maps show the calculated evolution of the visible and infrared spectra as the laser power is increased from zero to 3.2 W, with the upper axes showing the maximum-power spectra when both nonlinearities are present, or when just $\chi^{(2)}$ or $\chi^{(3)}$ is present. With both nonlinearities present, Fig. 4 shows that SPM broadens the input laser spectrum to span from 950–1250 nm; SHG then converts the most intense central components into the light at 520 nm that will act as a pump, while the weaker longer wavelengths seed the high-order parametric gain process. With $\chi^{(2)} = 0$, no frequency-doubled light is observed, while with $\chi^{(3)} = 0$, the input laser spectrum remains unbroadened, and no second-harmonic light of sufficiently long wavelength is available to seed the supercontinuum process.

The NEE model, while elucidating the processes responsible for supercontinuum generation, exhibits power distributions within the fundamental and supercontinuum spectra that differ from those observed experimentally by showing stronger

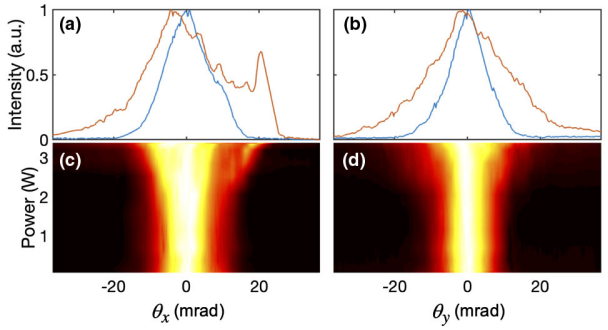

Fig. 5. Profiles of the fundamental beam after the OPGaP crystal, showing a power-dependent self-defocusing effect, which we attribute to cascaded second-order effects. Panels (a) and (b) show, respectively, the x and y beam profiles at minimum (blue) and maximum (red) powers. The corresponding color maps show the beam intensity on a linear scale, indicating a divergence that approximately doubles as the power is increased from 60 mW to 3.38 W.

SPM. Beam-profile data for the fundamental wavelength are presented in Fig. 5, revealing a power-dependent defocusing effect that cannot be explained by either Kerr self-focusing or thermal lensing, both of which imply positive lensing in GaP and would result in a tighter focus and stronger SPM than we observe. Instead, we attribute the weaker SPM to self-defocusing of the fundamental beam due to cascaded second-order effects [19]. Using the analysis presented in Ref. [20], it can be shown that $\chi^{(2)}(\omega; 2\omega, -\omega) : \chi^{(2)}(2\omega; \omega, \omega)$ cascading causes the fundamental beam to experience a peak nonlinear phase shift of -19 rad, corresponding to $n_2^{\text{eff}} \approx -6.2 \times 10^{-13}$ cm^2 W^{-1}, opposite in sign and nearly 10× larger than n_2 (Kerr) $= 6.5 \times 10^{-14}$ cm^2 W^{-1}. Strong negative defocusing is associated with this nonlinearity, leading to a self-limiting behavior that suppresses further SPM-driven spectral broadening. Extending the existing NEE model to a spatio-temporal simulation including thermal, Kerr, cascaded-$\chi^{(2)}$, and even photorefractive effects [21,22] would be needed to adequately capture the full dynamics of the supercontinuum process, but its accuracy would ultimately be limited by uncertainties in experimental and material parameters, e.g., grating nonuniformity.

Our assertion that parametric gain in the green is responsible for the supercontinuum generation process is further confirmed

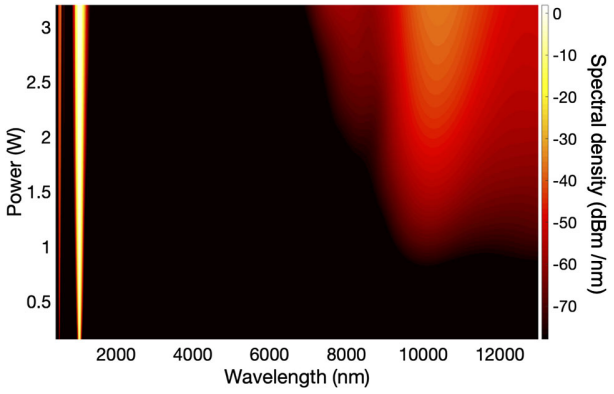

Fig. 6. Full-spectrum NEE simulation, showing long-wave infrared generation above 7 μm, corresponding to idler radiation from difference-frequency mixing between 520 nm and wavelengths shorter than 562 nm.

in Fig. 6, which illustrates the long-wave infrared generation observed in the NEE model above powers where SPM broadens the spectrum to a range sufficient to generate the necessary seed wavelengths. Infrared generation occurs above 7 μm, corresponding to peak parametric gain below 562 nm, as observed experimentally. The exceptional properties of OPGaP, which combines a phase-matchable $\chi^{(2)}$ nonlinearity with a high $\chi^{(3)}$ nonlinearity and simultaneous transmission in the visible and long-wave infrared, make it uniquely suitable for such an intra-pulse supercontinuum process. Indeed, optical parametric oscillation pumped at 1.04 μm has been reported at wavelengths extending to 13.5 μm [23], and OPGaP's transparency extends to 17 μm, with the exception of an absorption around 14 μm.

In summary, we have reported the first example of supercontinuum generation in a bulk nonlinear crystal pumped by a high-repetition-rate femtosecond laser oscillator. Visible light generation is a result of 520 nm pumped parametric gain, which amplifies weak SPM sidebands while simultaneously generating long-wavelength idler light. A power-dependent defocusing effect observed in tandem with supercontinuum generation is attributed to cascaded second-order effects in the OPGaP crystal, and it serves to self-limit the amount of SPM-induced spectral broadening in the crystal. With the ready possibility of using engineered quasi-phase-matching to enhance the high-order effects responsible for supercontinuum generation, it may be possible to reduce the average power needed to levels where greater spectral broadening is achieved along with reduced parasitic effects.

Funding. Engineering and Physical Sciences Research Council (EP/R033013/1, EP/P005446/1).

Acknowledgment. The authors thank F. Biancalana (Heriot-Watt University) for helpful discussions in the preparation of this paper.

Disclosures. The authors declare no conflicts of interest.

REFERENCES

1. J. A. Armstrong, N. Bloembergen, J. Ducuing, and P. S. Pershan, Phys. Rev. A **127**, 1918 (1962).
2. C. Langrock, M. M. Fejer, I. Hartl, and M. E. Fermann, Opt. Lett. **32**, 2478 (2007).
3. C. R. Phillips, C. Langrock, J. S. Pelc, M. M. Fejer, I. Hartl, and M. E. Fermann, Opt. Express **19**, 18754 (2011).
4. C. R. Phillips, C. Langrock, J. S. Pelc, M. M. Fejer, J. Jiang, M. E. Fermann, and I. Hartl, Opt. Lett. **36**, 3912 (2011).
5. C. B. Ebert, L. A. Eyres, M. M. Fejer, and J. S. Harris, Jr., J. Cryst. Growth **201–202**, 187 (1999).
6. T. Matsushita, T. Yamamoto, and T. Kondo, Jpn. J. Appl. Phys. **46**, L408 (2007).
7. Q. Ru, K. Zhong, N. P. Lee, Z. E. Loparo, P. G. Schunemann, S. Vasilyev, S. B. Mirov, and K. L. Vodopyanov, Proc. SPIE **10088**, 1008809 (2017).
8. L. Maidment, P. G. Schunemann, and D. T. Reid, Opt. Lett. **41**, 4261 (2016).
9. L. A. Pomeranz, P. G. Schunemann, D. J. Magarrell, J. C. McCarthy, K. T. Zawilski, and D. E. Zelmon, Proc. SPIE **9347**, 93470K (2015).
10. J. Wei, J. M. Murray, J. O. Barnes, D. M. Krein, P. G. Schunemann, and S. Guha, Opt. Mater. Express **8**, 485 (2018).
11. M. Conforti, F. Baronio, and C. De Angelis, Phys. Rev. A **81**, 053841 (2010).
12. M. Conforti, F. Baronio, C. De Angelis, M. Marangoni, and G. Cerullo, J. Opt. Soc. Am. B **28**, 892 (2011).
13. S. Wabnitz and V. V. Kozlov, J. Opt. Soc. Am. B **27**, 1707 (2010).
14. F. Baronio, M. Conforti, C. De Angelis, D. Modotto, S. Wabnitz, M. Andreana, A. Tonello, P. Leproux, and V. Couderc, Opt. Fiber Technol. **18**, 283 (2012).
15. M. Conforti, F. Baronio, and C. De Angelis, IEEE Photon. J. **2**, 600 (2010).
16. D. F. Parsons and P. D. Coleman, Appl. Opt. **10**, 1683 (1971).
17. P. J. Dean and D. G. Thomas, Phys. Rev. **150**, 690 (1966).
18. F. Liu, Y. Li, Q. Xing, L. Chai, M. Hu, C. Wang, Y. Deng, Q. Sun, and C. Wang, J. Opt. **12**, 95201 (2010).
19. L. A. Ostrovskii, JETP Lett. **5**, 272 (1967).
20. R. DeSalvo, H. Vanherzeele, D. J. Hagan, M. Sheik-Bahae, G. Stegeman, and E. W. Van Stryland, Opt. Lett. **17**, 28 (1992).
21. J. Feinberg, J. Opt. Soc. Am. **72**, 46 (1982).
22. K. Kuroda, Y. Okazaki, T. Shimura, H. Okamura, M. Chihara, M. Itoh, and I. Ogura, Opt. Lett. **15**, 1197 (1990).
23. L. Maidment, O. Kara, P. G. Schunemann, J. Piper, K. McEwan, and D. T. Reid, Appl. Phys. B **124**, 143 (2018).

Bibliography

[1] I Hartl, XD Li, C Chudoba, et al. “Ultrahigh-resolution optical coherence tomography using continuum generation in an air–silica microstructure optical fiber”. In: *Optics letters* 26.9 (2001), pp. 608–610.

[2] Yuan Liu, Haohua Tu, and Stephen A Boppart. “Wave-breaking-extended fiber supercontinuum generation for high compression ratio transform-limited pulse compression”. In: *Optics letters* 37.12 (2012), pp. 2172–2174.

[3] Th Udem, Ronald Holzwarth, and Theodor W Hänsch. “Optical frequency metrology”. In: *Nature* 416.6877 (2002), pp. 233–237.

[4] Christoph Gohle, Thomas Udem, Maximilian Herrmann, et al. “A frequency comb in the extreme ultraviolet”. In: *Nature* 436.7048 (2005), pp. 234–237.

[5] JM Langridge, T Laurila, RS Watt, et al. “Cavity enhanced absorption spectroscopy of multiple trace gas species using a supercontinuum radiation source”. In: *Optics Express* 16.14 (2008), pp. 10178–10188.

[6] John M Dudley and Stéphane Coen. “Coherence properties of supercontinuum spectra generated in photonic crystal and tapered optical fibers”. In: *Optics letters* 27.13 (2002), pp. 1180–1182.

[7] Norihiko Nishizawa, Toshiki Niinomi, Yoshitaka Nomura, et al. “Octave Spanning Coherent Supercontinuum Comb Generation Based on Er-Doped Fiber Lasers and Their Characterization”. In: *IEEE Journal of Selected Topics in Quantum Electronics* 24.3 (2017), pp. 1–9.

[8] Jinendra K Ranka, Robert S Windeler, and Andrew J Stentz. “Visible continuum generation in air–silica microstructure optical fibers with anomalous dispersion at 800 nm”. In: *Optics letters* 25.1 (2000), pp. 25–27.

[9] Michael RE Lamont, Barry Luther-Davies, Duk-Yong Choi, et al. “Supercontinuum generation in dispersion engineered highly nonlinear (γ= 10/W/m) As 2 S 3 chalcogenide planar waveguide”. In: *Optics Express* 16.19 (2008), pp. 14938–14944.

[10] Alexander C Judge, Stephen A Dekker, Ravi Pant, et al. “Soliton self-frequency shift performance in As 2 S 3 waveguides”. In: *Optics express* 18.14 (2010), pp. 14960–14968.

[11] Dong Yoon Oh, David Sell, Hansuek Lee, et al. “Supercontinuum generation in an on-chip silica waveguide”. In: *Optics letters* 39.4 (2014), pp. 1046–1048.

[12] Rai Kou, Taiki Hatakeyama, Jason Horng, et al. “Mid-IR broadband supercontinuum generation from a suspended silicon waveguide”. In: *Optics letters* 43.6 (2018), pp. 1387–1390.

[13] Minghui Yang, Yuhao Guo, Jing Wang, et al. “Mid-IR supercontinuum generated in low-dispersion Ge-on-Si waveguides pumped by sub-ps pulses”. In: *Optics express* 25.14 (2017), pp. 16116–16122.

[14] Lin Zhang, Yan Yan, Yang Yue, et al. “On-chip two-octave supercontinuum generation by enhancing self-steepening of optical pulses”. In: *Optics express* 19.12 (2011), pp. 11584–11590.

[15] Dmitry Martyshkin, Vladimir Fedorov, Taylor Kesterson, et al. “Visible-near-middle infrared spanning supercontinuum generation in a silicon nitride (Si 3 N 4) waveguide”. In: *Optical Materials Express* 9.6 (2019), pp. 2553–2559.

[16] Carsten Langrock, MM Fejer, I Hartl, et al. “Generation of octave-spanning spectra inside reverse-proton-exchanged periodically poled lithium niobate waveguides”. In: *Optics letters* 32.17 (2007), pp. 2478–2480.

[17] CR Phillips, Carsten Langrock, JS Pelc, et al. “Supercontinuum generation in quasi-phasematched waveguides”. In: *Optics express* 19.20 (2011), pp. 18754–18773.

[18] CR Phillips, Carsten Langrock, JS Pelc, et al. “Supercontinuum generation in quasi-phase-matched LiNbO 3 waveguide pumped by a Tm-doped fiber laser system”. In: *Optics letters* 36.19 (2011), pp. 3912–3914.

[19] Christopher B Ebert, Loren A Eyres, Martin M Fejer, et al. “MBE growth of antiphase GaAs films using GaAs/Ge/GaAs heteroepitaxy”. In: *Journal of crystal growth* 201 (1999), pp. 187–193.

[20] Tomonori Matsushita, Takahisa Yamamoto, and Takashi Kondo. “Epitaxial growth of spatially inverted GaP for quasi phase matched nonlinear optical devices”. In: *Japanese journal of applied physics* 46.5L (2007), p. L408.

[21] Qitian Ru, Kai Zhong, Nathaniel P Lee, et al. “Instantaneous spectral span of 2.85-8.40 μm achieved in a Cr: ZnS laser pumped subharmonic OPO”. In: *Nonlinear Frequency Generation and Conversion: Materials and Devices XVI*. Vol. 10088. International Society for Optics and Photonics. 2017, p. 1008809.

[22] Luke Maidment, Peter G Schunemann, and Derryck T Reid. “Molecular fingerprint-region spectroscopy from 5 to 12 μm using an orientation-patterned gallium phosphide optical parametric oscillator”. In: *Optics letters* 41.18 (2016), pp. 4261–4264.

[23] Leonard A Pomeranz, Peter G Schunemann, Daniel J Magarrell, et al. “1-micron-pumped OPO based on orientation-patterned GaP”. In: *Nonlinear Frequency Generation and Conversion: Materials, Devices, and Applications XIV*. Vol. 9347. International Society for Optics and Photonics. 2015, 93470K.

[24] Robert W Boyd. *Nonlinear optics*. Academic press, 2019.

[25] N. Bloembergen, R. K. Chang, and C. H. Lee. “Second-Harmonic Generation of Light in Reflection from Media with Inversion Symmetry”. In: *Phys. Rev. Lett.* 16 (22 May 1966), pp. 986–989. DOI: 10.1103/PhysRevLett.16.986. URL: https://link.aps.org/doi/10.1103/PhysRevLett.16.986.

[26] Thomas Y. F. Tsang. “Optical third-harmonic generation at interfaces”. In: *Phys. Rev. A* 52 (5 Nov. 1995), pp. 4116–4125. DOI: 10.1103/PhysRevA.52.4116. URL: https://link.aps.org/doi/10.1103/PhysRevA.52.4116.

[27] J. A. Armstrong, N. Bloembergen, J. Ducuing, et al. “Interactions between Light Waves in a Nonlinear Dielectric”. In: *Phys. Rev.* 127 (6 Sept. 1962), pp. 1918–1939. DOI: 10.1103/PhysRev.127.1918. URL: https://link.aps.org/doi/10.1103/PhysRev.127.1918.

[28] F. Zernike and J.E. Midwinter. *Applied Nonlinear Optics*. Dover Books on Physics Series. Dover Publications, Incorporated, 2013. ISBN: 9780486788159. URL: https://books.google.de/books?id=XMbmwQEACAAJ.

[29] Carsten Langrock. *Classical and low-light-level detection and pulse characterization using optical-frequency mixers*. 2007.

[30] Ichiro Shoji, Takashi Kondo, Ayako Kitamoto, et al. “Absolute scale of second-order nonlinear-optical coefficients”. In: *JOSA B* 14.9 (1997), pp. 2268–2294.

[31] JH Bechtel and W Lee Smith. “Two-photon absorption in semiconductors with picosecond laser pulses”. In: *Physical Review B* 13.8 (1976), p. 3515.

[32] Shinji Koh, Takashi Kondo, Yasuhiro Shiraki, et al. “GaAs/Ge/GaAs sublattice reversal epitaxy and its application to nonlinear optical devices”. In: *Journal of crystal growth* 227 (2001), pp. 183–192.

[33] Shinji Koh, Takashi Kondo, Minoru Ebihara, et al. “GaAs/Ge/GaAs sublattice reversal epitaxy on GaAs (100) and (111) substrates for nonlinear optical devices”. In: *Japanese journal of applied physics* 38.5A (1999), p. L508.

[34] Peter G Schunemann, Scott D Setzler, Lee Mohnkern, et al. “2.05-μm-laser-pumped orientation-patterned gallium arsenide (OPGaAs) OPO”. In: *Conference on Lasers and Electro-Optics*. Optical Society of America. 2005, CThQ4.

[35] Peter G Schunemann, Lee Mohnkern, Alice Vera, et al. “All-epitaxial growth of orientation-patterned gallium phosphide (OPGaP)”. In: *Advances in Optical Materials*. Optical Society of America. 2012, ITh5B–5.

[36] Jean Wei, Joel M Murray, Jacob O Barnes, et al. “Temperature dependent Sellmeier equation for the refractive index of GaP”. In: *Optical Materials Express* 8.2 (2018), pp. 485–490.

[37] Govind P Agrawal. “Nonlinear fiber optics”. In: *Nonlinear Science at the Dawn of the 21st Century*. Springer, 2000, pp. 195–211.

[38] AD Buckingham. “Birefringence resulting from the application of an intense beam of light to an isotropic medium”. In: *Optical, Electric and Magnetic Properties of Molecules*. Elsevier, 1997, pp. 264–269.

[39] PD Maker, RW Terhune, and CM Savage. “Intensity-dependent changes in the refractive index of liquids”. In: *Physical Review Letters* 12.18 (1964), p. 507.

[40] JH Marburger. “Self-focusing: theory”. In: *Progress in quantum electronics* 4 (1975), pp. 35–110.

[41] Yuen-ron Shen. “Self-focusing: experimental”. In: *Progress in quantum electronics* 4 (1975), pp. 1–34.

[42] A Dubietis, A Couairon, E Kučinskas, et al. “Measurement and calculation of nonlinear absorption associated with femtosecond filaments in water”. In: *Applied Physics B* 84.3 (2006), pp. 439–446.

[43] A Becker, N Aközbek, K Vijayalakshmi, et al. “Intensity clamping and re-focusing of intense femtosecond laser pulses in nitrogen molecular gas”. In: *Applied physics B* 73.3 (2001), pp. 287–290.

[44] W Liu, S Petit, A Becker, et al. “Intensity clamping of a femtosecond laser pulse in condensed matter”. In: *Optics Communications* 202.1-3 (2002), pp. 189–197.

[45] Martin M Fejer, GA Magel, Dieter H Jundt, et al. “Quasi-phase-matched second harmonic generation: tuning and tolerances”. In: *IEEE Journal of Quantum Electronics* 28.11 (1992), pp. 2631–2654.

[46] C Conti, Stefano Trillo, P Di Trapani, et al. “Effective lensing effects in parametric frequency conversion”. In: *JOSA B* 19.4 (2002), pp. 852–859.

[47] Miroslav Kolesik and Jerome V Moloney. “Nonlinear optical pulse propagation simulation: From Maxwell’s to unidirectional equations”. In: *Physical Review E* 70.3 (2004), p. 036604.

[48] Moloney Kolesik, Jerome V Moloney, and M Mlejnek. “Unidirectional optical pulse propagation equation”. In: *Physical review letters* 89.28 (2002), p. 283902.

[49] AV Husakou and J Herrmann. “Supercontinuum generation of higher-order solitons by fission in photonic crystal fibers”. In: *Physical Review Letters* 87.20 (2001), p. 203901.

[50] Himadri S Chakraborty, Mette B Gaarde, and Arnaud Couairon. “Single attosecond pulses from high harmonics driven by self-compressed filaments”. In: *Optics letters* 31.24 (2006), pp. 3662–3664.

[51] Mette B Gaarde and Arnaud Couairon. “Intensity spikes in laser filamentation: diagnostics and application”. In: *Physical review letters* 103.4 (2009), p. 043901.

[52] Michael Geissler, Gabriel Tempea, Armin Scrinzi, et al. “Light propagation in field-ionizing media: extreme nonlinear optics”. In: *Physical review letters* 83.15 (1999), p. 2930.

[53] Arnaud Couairon and André Mysyrowicz. “Femtosecond filamentation in transparent media”. In: *Physics reports* 441.2-4 (2007), pp. 47–189.

[54] Paul Kinsler and GHC New. “Few-cycle pulse propagation”. In: *Physical Review A* 67.2 (2003), p. 023813.

[55] Miguel A Porras. “Propagation of single-cycle pulsed light beams in dispersive media”. In: *Physical Review A* 60.6 (1999), p. 5069.

[56] Thomas Brabec and Ferenc Krausz. “Nonlinear optical pulse propagation in the single-cycle regime”. In: *Physical Review Letters* 78.17 (1997), p. 3282.

[57] Jerome V Moloney and Alan C Newell. *Nonlinear optics*. Westview Press, 2004.

[58] Matteo Conforti, Fabio Baronio, and Costantino De Angelis. “Nonlinear envelope equation for broadband optical pulses in quadratic media”. In: *Physical Review A* 81.5 (2010), p. 053841.

[59] M Conforti, F Baronio, C De Angelis, et al. “Theory and experiments on multistep parametric processes in nonlinear optics”. In: *JOSA B* 28.4 (2011), pp. 892–895.

[60] S Wabnitz and VV Kozlov. “Harmonic and supercontinuum generation in quadratic and cubic nonlinear optical media”. In: *JOSA B* 27.9 (2010), pp. 1707–1711.

[61] Feng Liu, Yanfeng Li, Qirong Xing, et al. “Three-photon absorption and Kerr nonlinearity in undoped bulk GaP excited by a femtosecond laser at 1040 nm”. In: *Journal of Optics* 12.9 (2010), p. 095201.

[62] LA Ostrovskii. “Propagation of wave packets and space-time self-focusing in a nonlinear medium”. In: *Sov. Phys. JETP* 24.4 (1967), pp. 797–800.

[63] Richard DeSalvo, David J Hagan, Mansoor Sheik-Bahae, et al. “Self-focusing and self-defocusing by cascaded second-order effects in KTP”. In: *Optics letters* 17.1 (1992), pp. 28–30.

[64] Jack Feinberg. “Asymmetric self-defocusing of an optical beam from the photorefractive effect”. In: *JOSA* 72.1 (1982), pp. 46–51.

[65] Kezao Kuroda, Y Okazaki, T Shimura, et al. “Photorefractive effect in GaP”. In: *Optics letters* 15.21 (1990), pp. 1197–1199.